Cell driven elastomeric particle packing in composite bioinks for engineering and implantation of stable 3D printed structures

Shira Landau [a,b,c,1], Jennifer Kieda [a,b,c,1], Ramak Khosravi [b,d], Sargol Okhovatian [a,b,c], Kaitlyn Ramsay [a,b,c], Chuan Liu [a,b,c], Amid Shakeri [a,b,c], Yimu Zhao [a,b,c,i], Karen Shen [a,b,c], Orit Bar-Am [g], Shulamit Levenberg [g], Scott Tsai [e,f], Milica Radisic [a,b,c,h,i,*]

[a] University of Toronto, Institute of Biomedical Engineering, Toronto, ON, Canada
[b] University Health Network, Toronto General Hospital Research Institute, Toronto, ON, Canada
[c] University of Toronto, Terrence Donnelly Centre for Cellular & Biomolecular Research, Toronto, ON, Canada
[d] Division of Cardiovascular and Thoracic Surgery, Department of Surgery, Duke University Medical Center, Durham, NC, United States
[e] Toronto Metropolitan University, Department of Mechanical, Industrial, and Mechatronics Engineering, Toronto, ON, Canada
[f] Toronto Metropolitan University and Unity Health Toronto, Institute for Biomedical Engineering, Science and Technology (iBEST), Toronto, ON, Canada
[g] Faculty of Biomedical Engineering, Technion, Haifa, IL, Israel
[h] University of Toronto, Department of Chemical Engineering and Applied Chemistry, Toronto, ON, Canada
[i] Acceleration Consortium, University of Toronto, Toronto, ON, Canada

ARTICLE INFO

ABSTRACT

Geometric and structural integrity often deteriorate in 3D printed cell-laden constructs over time due to cellular compaction and hydrogel shrinkage. This study introduces a new approach that synergizes the advantages of cell compatibility of biological hydrogels and mechanical stability of elastomeric polymers for structure fidelity maintenance upon stereolithography and extrusion 3D printing. Enabling this advance is the composite bioink, formulated by integrating elastomeric microparticles from poly(octamethylene maleate (anhydride) citrate) (POMaC) into biologically derived hydrogels (fibrin, gelatin methacryloyl (GelMA), and alginate). The composite bioink enhanced the elasticity and plasticity of the 3D printed constructs, effectively mitigating tissue compaction and swelling. It exhibited a low shear modulus and a rapid crosslinking time, along with a high ultimate compressive strength and resistance to deformation from cellular forces and physical handling; this was attributed to packing and stress dissipation of elastomeric particles, which was confirmed via mathematical modelling. Enhanced functional assembly and stability of human iPSC-derived cardiac tissues and primary vasculature proved the utility of the composite bioink in tissue engineering. *In vivo* implantation studies revealed that constructs containing POMaC particles exhibited improved resilience against host tissue stress, enhanced angiogenesis, and infiltration of pro-reparative macrophages.

1. Introduction

3D printing allows for unprecedented control of construct structure at the μm-level, while at the same time precisely controlling the position of multiple cell types to create sophisticated structures matching those of native tissues [1]. Biological hydrogels are extensively utilized as bioinks for the 3D printing of cells due to their biocompatibility, the presence of defined cell-adhesion ligands, and biodegradability that allows for cell migration and largely favorable conditions for the transport of large and small molecules. Hydrogels are viscoelastic, similar to

native tissues [2], and generally have low shear modulus, in some cases exhibiting a shear thinning behaviour that allows for facile extrusion printing in the presence of cells [3]. Hydrogels such as fibrin [4], gelatin methacryloyl (GelMA) [5,6], and collagen methacryloyl (ColMA) [7] are considered the gold standard for the biofabrication of a variety of structures for numerous applications [8]. For example, GelMA has attracted significant attention for its wide application in tissue engineering, particularly for vascularization [9] and cardiac [10] tissue engineering, its use as a bioink for 3D printing [11], and in regenerative medicine as an adhesive ink for wound healing [12].

Although these materials are compatible with cells, tractional forces resulting from adherent cells such as fibroblasts or myoblasts tend to compact them [13], which results in the deterioration of the original 3D-printed form [14]. Furthermore, 3D constructs that incorporate cells and are intended for *in vivo* implantation will encounter even greater stress within the host tissue environment [1] and ultimate shape distortion, which eliminates the benefits of the original 3D printing process. Vascularization and *in vivo* integration of such constructs remain a challenge.

In contrast, polymers like polycaprolactone (PCL) [15], poly (lactic-co-glycolic acid) (PLGA) [16] or polydimethylsiloxane (PDMS) [13] offer unprecedented structural control and stability during tissue cultivation, yet they cannot be fully impregnated with cells and generally suffer from unphysiologically high mechanical properties and poor permeability that is limited only to gases and small molecules. Their 3D printing often necessitates conditions such as elevated temperature or the use of organic solvents [17], which are unsuitable for live cell printing. Additionally, these types of polymers do not fully replicate the natural cellular environment due to their inherently high elasticity, with Young's modulus ranging from 0.4 to 7 GPa [18] versus 20–800 kPa

[19] for soft tissues.

Some of these limitations can be overcome through the use of UV-crosslinkable polymeric elastomers [20], which have elasticity in the range of native tissues [21] and compatibility with microscale processing techniques such as 3D stamping [22] and 3D printing [23–25]. Yet, they, too, suffer from poor permeability and the inability to fully impregnate the volume of the tissue with cells. Additionally, polymeric elastomers exhibit too long of a UV-crosslinking time for high-resolution stereolithographic printing and distort too much in extrusion printing [26,27].

Another way to enhance the functionality of hydrogel bioinks is by integrating synthetic materials into native hydrogels. This approach aims to strengthen the bioinks while preserving their cell printability. In recent studies, researchers have incorporated PLGA nanoparticles into alginate substrates to improve both the mechanical properties and the printability of the resulting bioink [28]. However, this approach inevitably alters the chemical properties of the bulk hydrogels, complicating their receptor-ligand interactions with living cells.

Here, we present an approach that combines the benefits of biological hydrogels and elastomeric polymers in a single composite granular bioink suitable for both stereolithography and extrusion 3D printing (Fig. 1). By incorporating elastomeric microparticles into biologically derived hydrogels, we engineered a bioink with unaltered cell-facing biological properties afforded by natural hydrogels and, at high strains, mechanical properties akin to those of polymeric elastomers (Fig. 1a). The elastomeric particles were generated in bulk and droplet microfluidic approaches from a UV-crosslinkable elastomer, POMaC, synthesized by polycondensation from citric acid, maleic anhydride, and 1,8-octanediol [21]. This cell-compatible elastomer has been previously employed as a scaffold to support cells in cardiac tissue engineering and
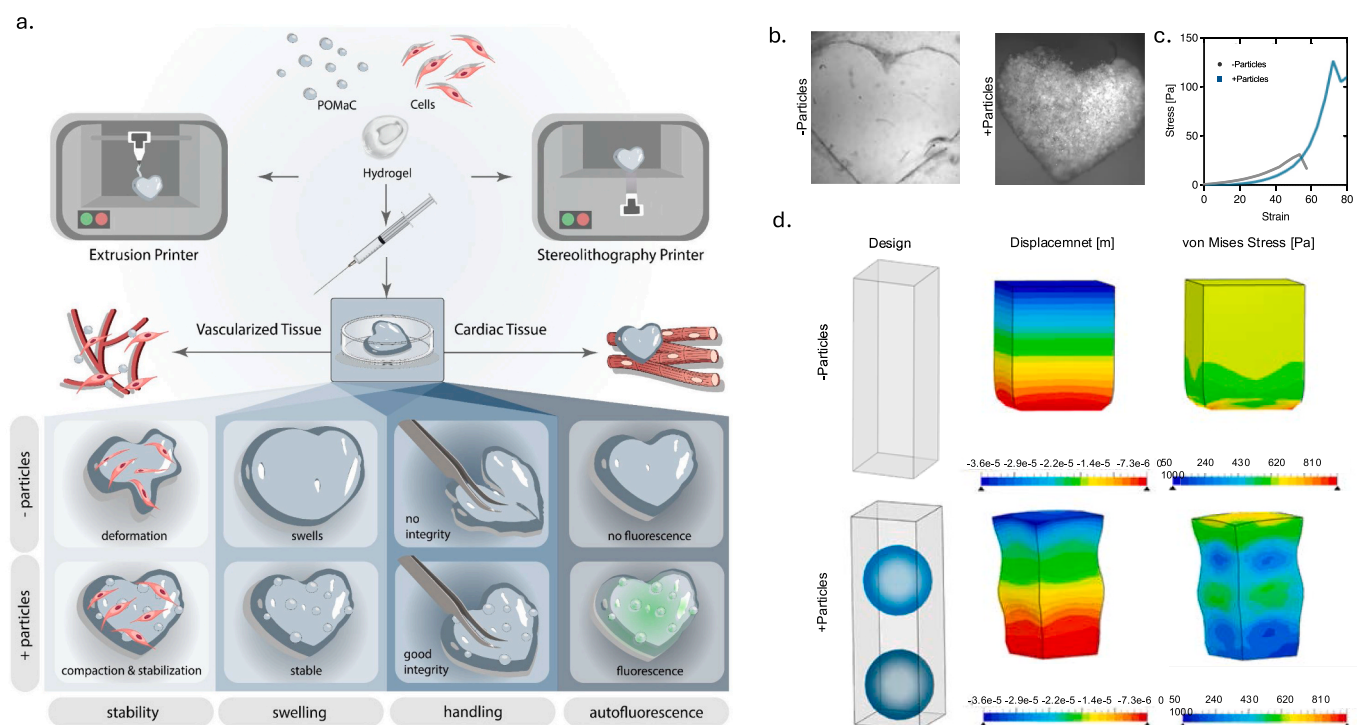

Fig. 1. Elastomeric particle packing in composite hydrogel bionks for stabilization of 3D printed structures. a) The integration of elastomeric POMaC particles with diverse hydrogels to formulate a bioink suitable for 3D printing via various printing and crosslinking methodologies. The presence of POMaC particles enhances the structural stability of the cell-incorporated constructs, mitigates the typical swelling associated with hydrogel use, and facilitates more convenient manipulation, specifically in terms of tweezer handling while maintaining the favorable cell-oriented hydrogel environment. The autofluorescence characteristics of POMaC enhance the ability to visualize the scaffold. POMaC particles can also facilitate tissue formation, as demonstrated by their addition to cardiac and vascularized tissues. **b)** 3D printed GelMA heart structures without (left) and incorporating POMaC particles (right), **c)** Stress-strain curves of hydrogel constructs with and without POMaC particles emphasizing higher ultimate compressive strength of particle-laden constructs. **d)** Finite element modelling of stress profiles as a function of displacement in hydrogels with and without POMAC particles.

allows for the creation of organ-on-a-chip models *in vitro* and implanted pressure sensors *in vivo* [29]. Furthermore, POMaC has been utilized to produce AngioChip, a platform that facilitates *in vitro* vascularization [30,31].

Our study revealed that the incorporation of POMaC particles into hydrogels increased not only the elasticity of the 3D printed constructs compared to controls without particles, but also their plasticity while concurrently reducing tissue compaction and swelling. The resulting ink had a low shear modulus and a fast crosslinking time similar to the base hydrogel to enable facile 3D printing. Yet, it had a high ultimate compressive strength. It also resisted swelling and compression from cellular tractional forces as well as construct handling better than hydrogels alone due to the packing of elastomer particles that enabled maintenance of the 3D-printed construct shape, ultimately enhancing the assembly of cardiac and vascular structures *in vitro*. The long-term *in vivo* implantation study demonstrated improved angiogenesis and pro-reparative macrophage infiltration with the bioink incorporating POMaC particles.

2. Results

2.1. Composite granular material for shape stabilization in 3D printing

Embedding POMaC particles in various hydrogels – specifically, fibrin, GelMA, and alginate – created versatile granular bioinks that supported remodeling and improved tissue generation by stromal cells, fibroblasts, and human iPSC-derived cardiomyocytes and enhanced vasculature formation while adding fluorescence for construct labelling (Fig. 1a and b). The results of micromechanical compression testing indicated that the composite material exhibited a behaviour akin to its parent hydrogel over a large range of strains (Fig. 1b), which facilitated extrusion 3D printing. Shear compression testing revealed that at low strains, the deformation was transferred mostly through the hydrogel component, and the composite granular bioink exhibited mechanical properties nearly identical to its parent hydrogel (Fig. 1c). Yet, as the compressive shear strain increased, the deformation carried through the hydrogel, bringing the elastomeric particles into contact with one another, which pushed back against the applied deformation (Fig. 1c). Thus, the composite bioink behaved like an elastic solid at higher strains, ultimately exhibiting a significantly higher ultimate tensile strength than its parent hydrogel (Fig. 1c). Finite element modelling demonstrated reduced von Mises stresses within the composite material, compared to the hydrogel alone when identical compressive displacement was applied to the structure (Fig. 1d), further supporting the ability of composite materials to resist compression. These bimodal mechanical properties enabled a unique behaviour of the granular composite material in cell culture and implantation.

2.2. POMaC particle generation using bulk and microfluidic methods

Elastomeric POMAC particles were fabricated from a linear pre-polymer that was characterized by NMR spectroscopy, FT-IR and rheometry (Fig. 2a–c). FT-IR analysis of UV crosslinked POMaC, in comparison to its liquid form, shows a reduction in the peaks located at 2929 cm^{-1} and 2863 cm^{-1}, indicating a lower presence of the alkyl groups from citric acid and 1,8-octanediol [32,33]. Similarly, the peaks of crosslinked POMaC were reduced at 1732 cm^{-1} and 1680 cm^{-1}, indicating a lower presence of the carbonyl groups from citric acid and the vinyl groups from maleic anhydride, respectively [33]. The reduced presence of these functional groups suggests their consumption during the crosslinking process [33]. Crosslinked POMaC exhibited a peak at 3462 cm^{-1} comparable to liquid POMaC, indicating a similar presence of hydroxyl groups (Fig. 2b).bb

POMaC particles were generated by mixing POMaC pre-polymer with polyethylene glycol dimethacrylate 500 (PEGDM) using bulk synthesis methods or microfluidic techniques (Fig. 2). For bulk synthesis, we used suspension polymerization by injecting POMaC polymer into a continuously stirred PVA solution. As a result, the POMaC pre-polymer spontaneously formed particles upon encapsulation by the PVA solution (Fig. 2d, S1 and Video S1-2). These particles were subsequently filtered for fractionation of desired sizes and UV-crosslinking (Fig. 2d).

We also employed droplet microfluidics as a proof of concept for the generation of monodisperse POMaC particles (Fig. 2ei and S2). We utilized a classical flow-focusing junction in a PDMS device (Fig. 2eii). To inhibit the adhesion and wetting of the highly viscous POMaC particles to the PDMS channels, a 20G syringe needle was laterally inserted through the PDMS chip, intersecting with the continuous phase channel. The particles were collected in a tube and subsequently crosslinked under UV light (Fig. 2ei and Video S3-5).

The resultant POMaC particles exhibited autofluorescence, rendering them advantageous for future applications (Fig. 2f). Scanning electron microscopy (SEM) images revealed that POMaC particles produced by microfluidics exhibited a higher degree of monodispersity compared to those produced by macro-scale production techniques (Fig. 2g). The size distribution of both microfluidic and macrofluidic POMaC particles, characterized by Tukey-Lambda distribution curves, elucidated the variance in particle uniformity between the two methods (Fig. 2h). Young's modulus measurements, performed with a micromechanical tester, showed no significant size or technique-dependent differences (Fig. 2i–k and S3).

2.3. Hybrid POMaC particles and hydrogel bioinks for 3D-printing

In pursuit of developing a bioink with superior mechanical stability for 3D printing applications that simultaneously preserves cell viability, we integrated POMaC particles with a variety of hydrogels. This bioink can also be enriched with cells and is compatible with various hydrogels (Fig. 3a). To ensure uniform particle distribution within the hydrogel constructs, it is essential to thoroughly mix the particle/hydrogel solution before printing. Particles tend to settle when left undisturbed in a tube for several minutes, which might lead to inconsistencies in the printed structures or, when using extrusion printing, to clogging of the nozzle (Figure S4).

First, we investigated the effect of particle size on the printability of PEGDA hydrogel structures by comparing constructs incorporating particles larger than 100 μm to those with particles smaller than 100 μm. Post-printing, the constructs were imaged, and the dissimilarity from the original print design was quantified. Within the range of conditions investigated, there were no significant differences, although a trend towards a greater dissimilarity was observed with larger particles and when particle concentration was decreased (Figure S5).

Scanning Electron Microscopy (SEM) analysis of 3D printed constructs from GelMA/POMaC particles and GelMA controls provided insights into the morphological changes imparted by the POMaC particles. It was observed that their inclusion introduced a desired textural complexity to the hydrogel matrix, which is likely to contribute to enhanced mechanical and cell adhesion properties (Fig. 3b).

Expanding the utility of the POMaC particle-enriched bioink, we explored its compatibility with different 3D printing modalities. Specifically, we conducted trials with stereolithography bioprinting, which is known for its high resolution and precision (Fig. 3ci-iii). Furthermore, we examined extrusion printing, which offers versatility and scalability and also excels in material diversity (Fig. 3civ-vi). Our results indicate that the hybrid bioink facilitated the fabrication of intricate structures while imparting autofluorescent properties to the constructs, which could be leveraged for imaging and tracking purposes post-printing (Fig. 3d). Additionally, we successfully demonstrated the printing capability of our bioink with a range of hydrogels, including fibrin, alginate, and GelMA (Fig. 3e).
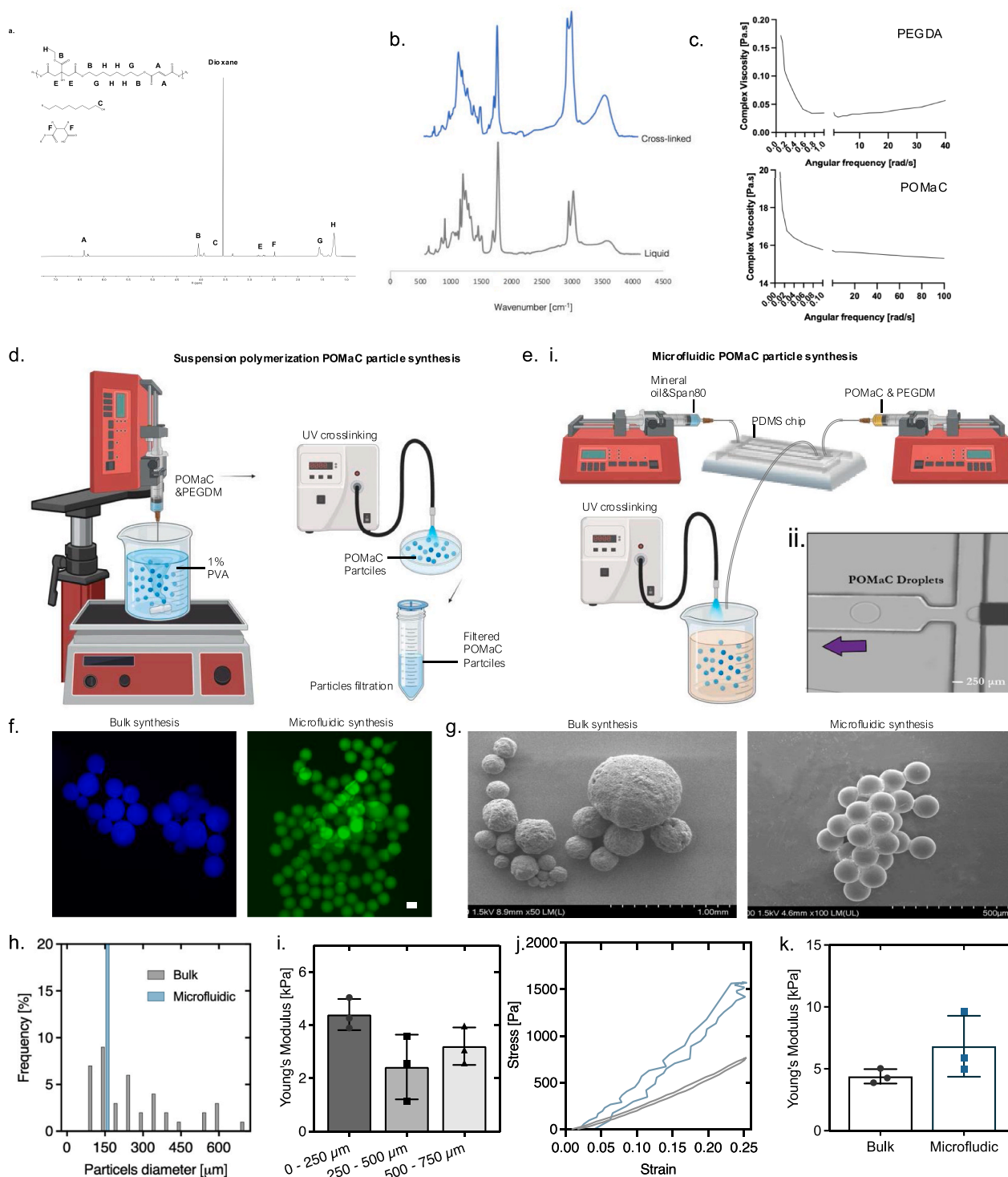
Fig. 2. Comparative analysis of POMaC particles fabricated by bulk and microfluidic approaches. **a)** Chemical structure of POMaC and its NMR spectroscopy data. **b)** FTIR analysis of POMaC in both its liquid and cross-linked forms. **c)** Viscoelastic characteristics of POMaC prepolymer and PEGDA demonstrated through rheometric measurement. **d)** Bulk fabrication process for POMaC particles, involving the injection of POMaC droplets via a syringe pump into a 1 % PVA solution under stirring, immediately followed by UV crosslinking to stabilize the particles and concluding with filtration and washing. **e-i)** Microfluidic production of POMaC droplets using a heated POMaC polymer dispensed by a syringe pump (dispersed phase) and light mineral oil with 2 % Span 80 (continuous phase). **e-ii)** The phases converge at a flow-focusing junction, indicated by a purple arrow, and exit through an outlet into a beaker for subsequent UV crosslinking. **f)** Representative fluorescence microscopy image of naturally autofluorescent POMaC particles, scale bar = 250 μm. **g)** Representative SEM images of POMaC particles demonstrating their morphology. **h)** Histogram of the particle size distribution for both bulk and microfluidic methods, based on 50 particles from each. **i)** Young's modulus of bulk POMaC particles across various size ranges, derived from the linear portion of the stress-strain curve in micromechanical measurements, with n = 3 samples per size group and one-way ANOVA using Tukey test. **j)** Representative stress-strain curves of POMaC particles from bulk and microfluidic processes measured by the microtester. **k)** Comparison of Young's modulus for bulk versus microfluidic POMaC particles, calculated from the linear range of the stress-strain curve, with n = 3 samples per method, unpaired two-tailed *t*-test. *P < 0.05 is considered significant. Data are shown as mean ± SD.
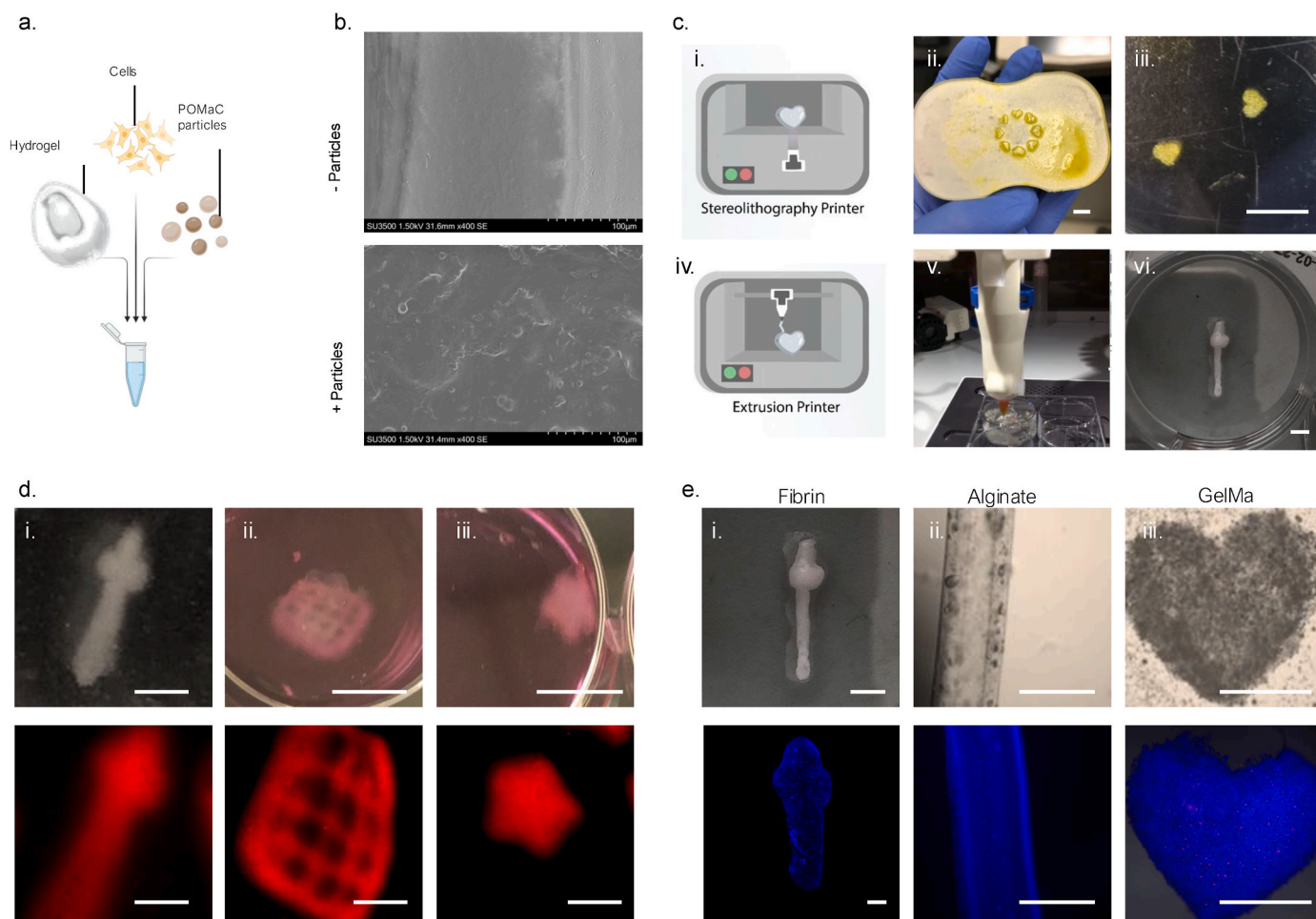
Fig. 3. Integration of POMaC particles into various hydrogels to create hybrid bioinks for diverse 3D printing applications. a) Schematic depiction of the hybrid bioink formulation, achieved by mixing POMaC particles with multiple biomaterials. **b)** Scanning Electron Microscope (SEM) images showcase the GelMA structures with and without POMaC particles, highlighting the additional texture conferred by the particles. **c)** The bioink is compatible with a variety of 3D printing techniques, including: **i-iii)** stereolithography and **iv-vi)** extrusion printing, scale bar = 1 cm. **d)** Diverse shapes were fabricated using extrusion-based 3D printing with fibrin/POMaC particles. Brightfield images are shown in the upper panel, while the lower panel displays the red fluorescent signal from Rhodamine-dextran tagged fibrinogen, along with the natural autofluorescence of POMaC particles. Scale bars = 5 mm for (i top), 3 mm for (i bottom), 1 cm for (ii top), 3 mm for (ii bottom), 1 cm for (iii top), and 3 mm for (iii bottom). **e)** Various structures were 3D printed using fibrin, alginate, and GelMA, each mixed with POMaC particles. The upper panel presents brightfield images, and the lower panel reveals the autofluorescence of POMaC particles in blue. Scale bars = 1 cm for (i top and bottom), 1 cm for (ii top), 5 mm for (ii bottom), 2 mm for (iii top and bottom).

2.4. Hybrid POMaC particles-hydrogel bioink enhance the mechanical characteristics of constructs
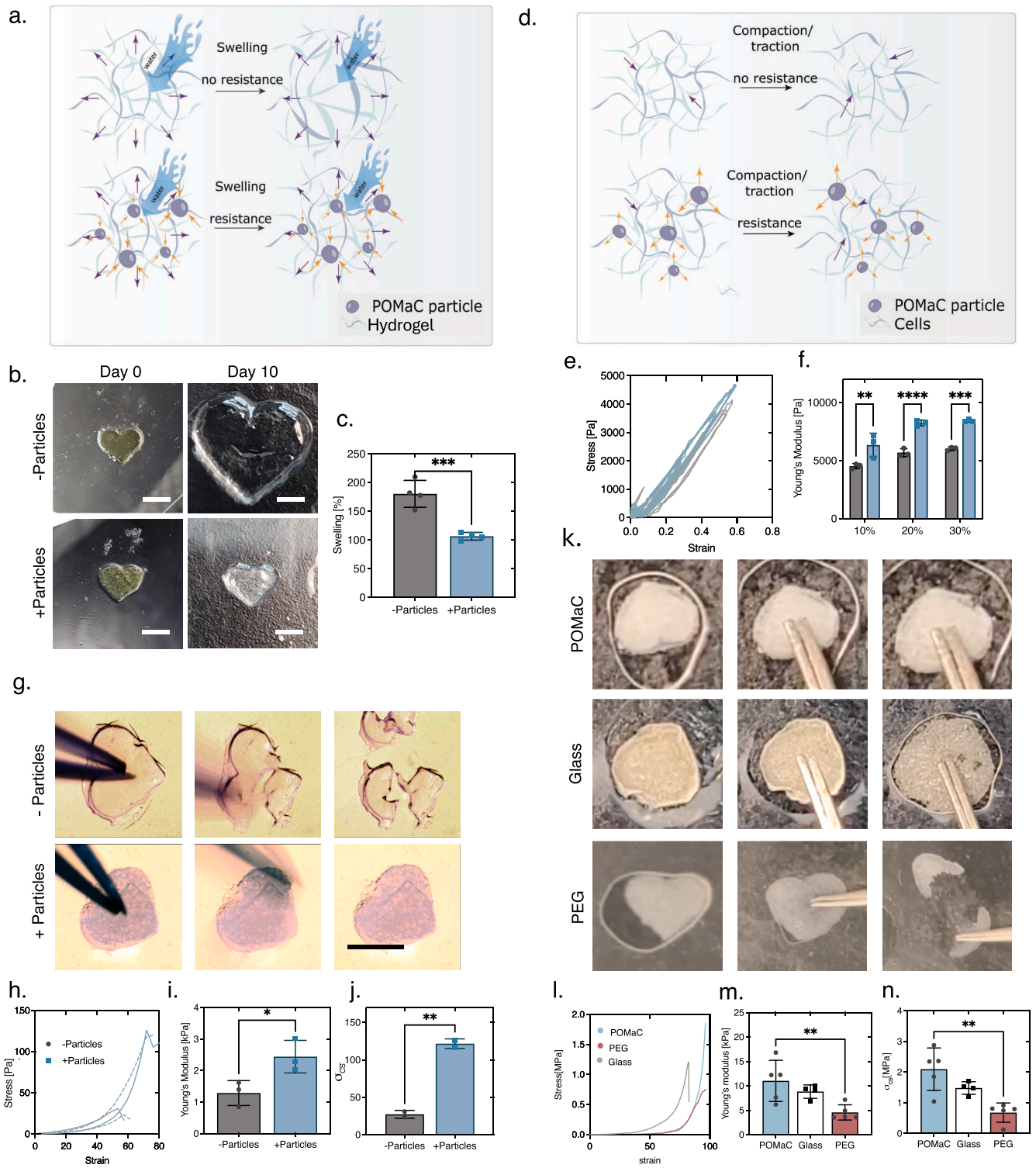
Adding POMaC particles into a PEGDA hydrogel reduced the degree of swelling observed in comparison to controls composed solely of PEGDA. We hypothesize that this reduction is attributable to the resistance imparted by the embedded particles within the hydrogel matrix (Fig. 4a–c). The measurements of Young's modulus using a micromechanical tester device showed that the elasticity of hybrid 3D-printed alginate constructs with particles was significantly higher than that of the control alginate-only constructs (Fig. 4d–f).

Tissue-engineered constructs must maintain their shape and remain intact during steps of manipulation required for cell seeding, cultivation, and *in vivo* implantation to ultimately retain their function *in vivo*. Our experiments demonstrated that the addition of particles to GelMA, followed by 3D printing, resulted in less brittle constructs (Fig. 4g and Video S6). This improvement was substantiated by compression testing (Fig. 4h and Video S7), where constructs containing POMaC particles exhibited a significantly higher Young's modulus (Fig. 4i) and a greater ultimate compressive strength (Fig. 4j).

In addition, we investigated the effect of particle size on the

mechanical properties of PEGDA/particle structures by comparing constructs incorporating particles larger than 100 μm to those with particles smaller than 100 μm. Our results demonstrate that incorporating larger particles with the hydrogel resulted in constructs that were overall softer and more brittle (Figure S6).

POMaC particles decreased the presence of dead cells and slowed down compaction of cell-laden hydrogels (Figure S7). An important question is whether the elasticity of the dispersed phase in the composite bioink is of paramount importance, or if the stability is indirectly provided by the enhanced granularity and topography that results from the incorporation of particles. To answer this question, we created composite bioinks consisting of control rigid glass or soft (polyethylene glycol) microparticles of comparable diameters to those of POMaC particles (75 μm for the glass particles and <100 μm for PEG particles (Figure S8)), incorporated into the GelMA hydrogel at identical concentrations. Manual handling tests showed glass beads added some structural stability to the composite constructs, albeit at lower levels to those observed with elastomeric POMaC microparticles. In contrast, constructs reinforced with microfluidically generated PEG microparticles failed to exhibit any stability and broke upon handling similarly to the non-reinforced GelMA hydrogels (Fig. 4k and Video S8-9). These

Fig. 4. The incorporation of POMaC particles within hydrogels increases their mechanical stability and control microparticles (rigid glass and soft hydrogel) in GelMA hydrogel fail to confer mechanical stability, demonstrating the advantage of elastomeric POMAC particles. a) Schematic of the reduced swelling that occurs when POMaC particles are incorporated within a hydrogel. **b)** Representative images of 3D-printed PEGDA constructs with and without POMaC particles, shown immediately after printing and 10 days post-printing, demonstrate the resistance to swelling provided by the particles. Scale bar = 4 mm. **c)** Swelling quantification of PEGDA/POMaC vs. PEGDA constructs. Data are represented as mean ± SD, with n ≥ 4 constructs per experiment. An unpaired two-tailed *t*-test was used, *P < 0.05. **d)** Schematic illustrating the contribution of POMaC particles to the increase in composite hydrogel stability. **e)** Stress-strain curve of Alginate/POMaC particles vs. Alginate-only tubes. **f)** Young's modulus of Alginate/POMaC particle tubes versus Alginate tubes, calculated from the linear range of the stress-strain curve. Data are represented as mean ± SD, with three constructs per experiment, unpaired two-tailed *t*-test, **P < 0.01, ***P < 0.001, ****P < 0.0001. **g)** Snapshots from tweezer handling videos comparing GelMA/POMaC particles with GelMA. **h)** Stress-strain curve of compression of cell-free GelMA printed constructs with and without POMaC particles measured by a Rheometer. **i)** Young's modulus of GelMA/POMaC particle structures versus GelMA structures, calculated from the linear range of the stress-strain curve. Data are represented as mean ± SD, with three constructs per experiment, unpaired two-tailed *t*-test, *P < 0.05. **j)** Ultimate compressive strength of GelMA/POMaC vs. GelMA, derived from the stress-strain curve presented in h. Data are represented as mean ± SD, with two constructs per experiment, unpaired two-tailed *t*-test, **P < 0.01. **k)** Representative images of construct stabilization during compression between two glass slides in POMAC composites versus the instability observed with hydrogel (PEG) and glass bead composites. **l)** Representative stress-strain curves from rheometer compression testing of the three composite types. **m)** Ultimate compression stress determined through rheometer compression tests. **n)** Young's modulus derived from the rheometer compression tests. Data are represented as mean ± SD, with n ≥ 4 constructs per experiment, one-way ANOVA with Tukey's test was used, **P < 0.01.

observations were substantiated with mechanical compression testing (Fig. 4l) that demonstrated superior ultimate compression strength (Fig. 4m) and Young's modulus (Fig. 4n) of the POMAC particle reinforced hydrogels in comparison to the two controls. Due to the rigidity of

glass microparticles, the composite bioink reinforced with them demonstrated a notably higher stress at identical strain levels compared to the POMaC and PEG-reinforced bioinks (Fig. 4l). The POMAC-reinforced bioink behaved identically to the PEG reinforced bioink
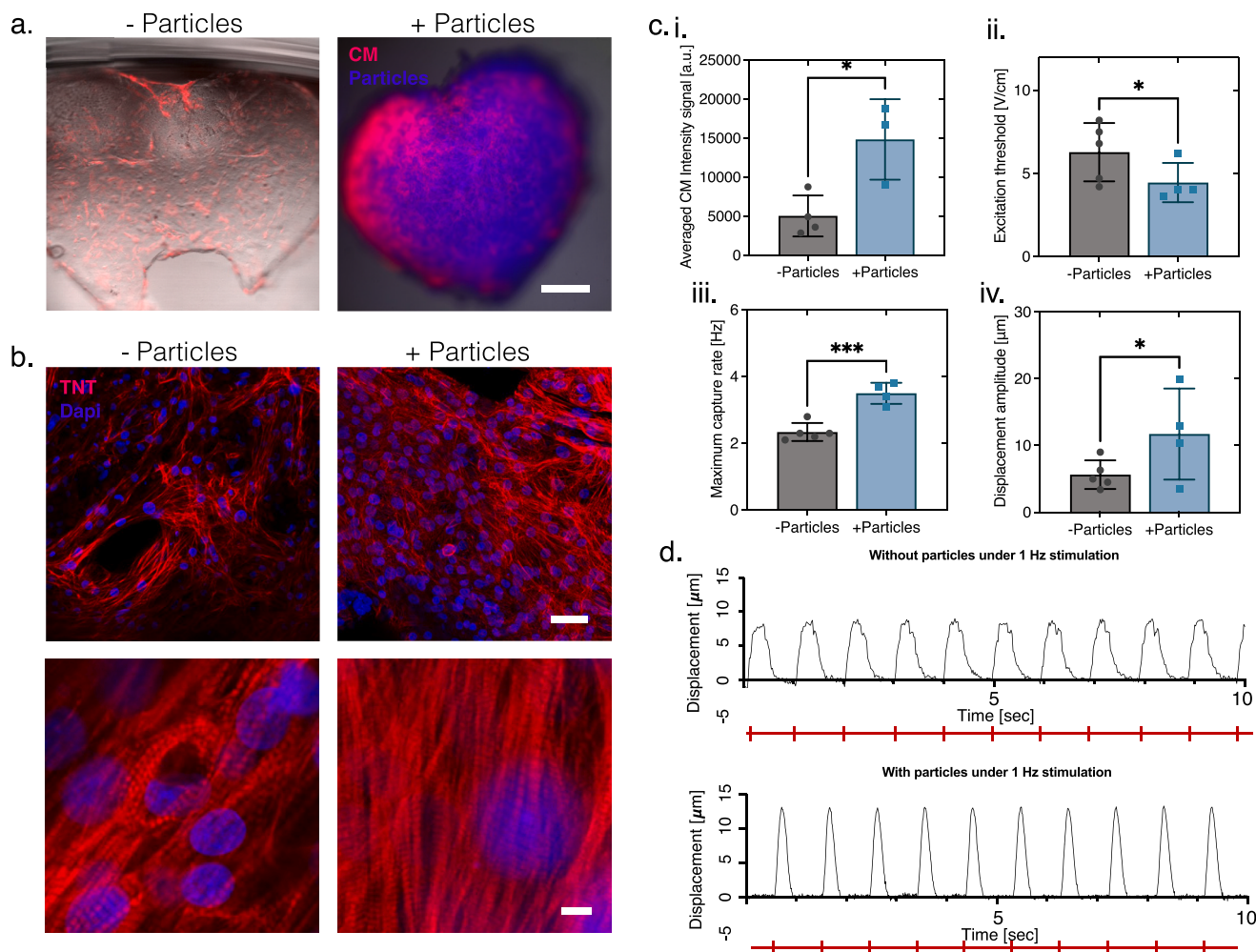

Fig. 5. Enhancement of Cardiomyocyte Attachment and Contractile Function in 3D-Printed GelMA Constructs by POMaC Particles. a) Representative images of 3D-printed GelMA constructs with and without POMaC particles, seeded with CMs. Red indicates GFP-expressing CMs; blue indicates the autofluorescence of POMaC particles. Scale = 3 mm. **b)** Representative images of troponin-T (TnT, red) and DAPI (blue) staining of 3D-printed GelMA constructs with and without POMaC particles, fixed on day 10 of culture. The upper and lower panels show lower and higher magnifications, respectively. Scale = 20 μm (upper images) and 25 μm (lower images). **c)** Functional assessment of cardiac tissues: **i.** CM coverage, calculated by the sum of positive fluorescent pixels; **ii.** Excitation threshold; **iii.** Maximum capture rate; and **iv.** Displacement amplitude. Data are presented as mean ± SD, with n ≥ 4 constructs per experiment. An unpaired two-tailed *t*-test was used, *P < 0.05, ***P < 0.001. **d)** Representative displacement traces of 3D-printed GelMA constructs seeded with CMs, under 1Hz stimulation, measured on day 10 of culture. Red lines indicate electrical stimuli.

over a large strain range, with the stress-strain profile governed largely by the hydrogel phase (Fig. 4l). Yet, at high strains, the reinforcement with elastomeric POMAC exhibited an ultimate compression strength nearly twice as high as that of the PEG-reinforced hydrogels (Fig. 4l).

To further validate the enhanced stability provided by the hybrid bioink, we implanted 3D-printed GelMA constructs, with and without particles, into the subcutaneous tissue of mice (Figures S9a-e). Ten days post-implantation, the grafts were examined (Figures S9c and d), and

the integrity of the constructs was quantified *in situ*. Constructs containing particles showed significantly higher *in situ* structural integrity compared to those without particles (Figure S9e).

2.5. POMaC particles incorporated in 3D-Printed GelMA constructs enhance Cardiomyocyte Attachment and Contractile Function

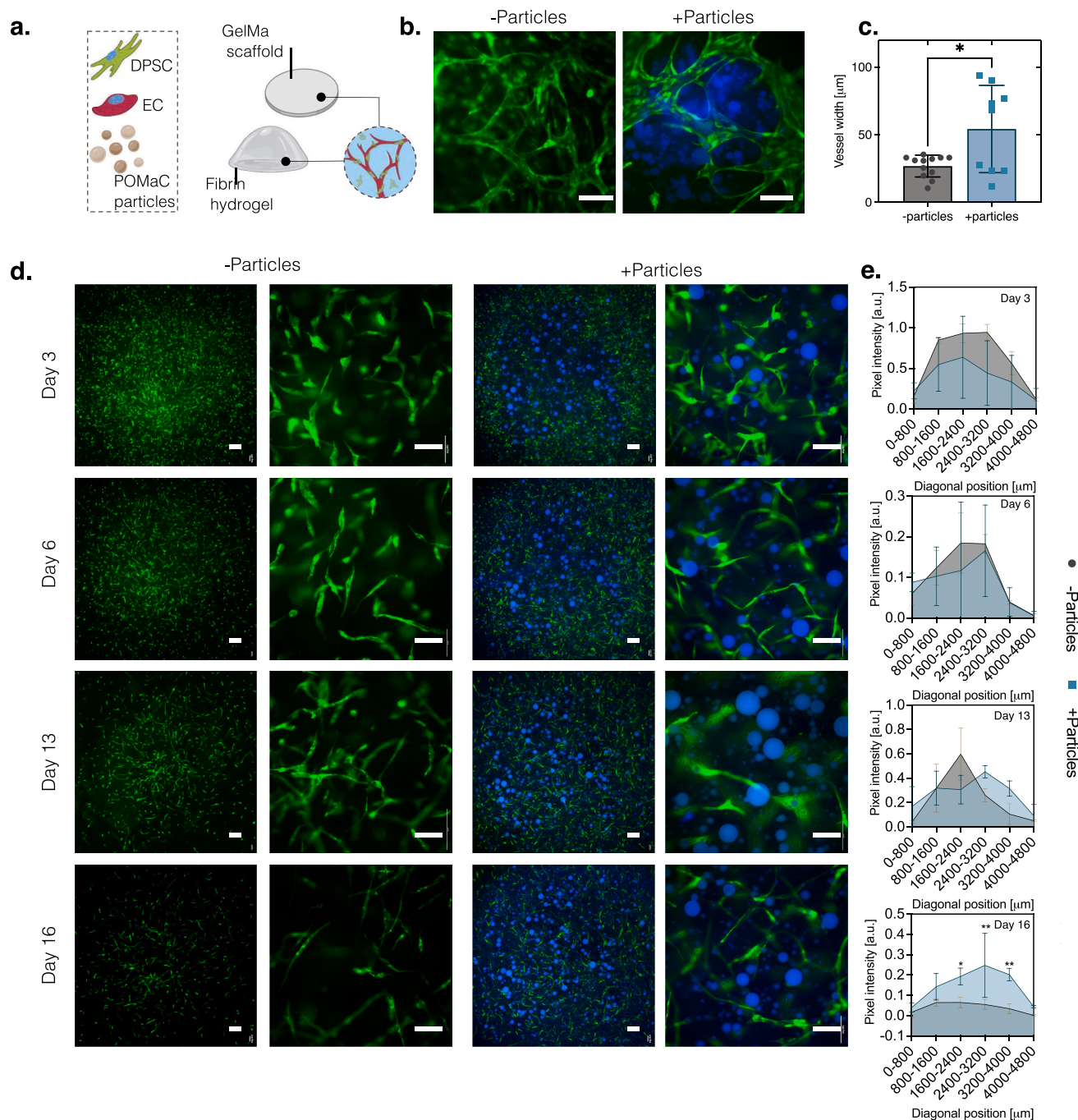We subsequently seeded human iPSC-derived cardiomyocytes (CMs)

Fig. 6. Effects of POMaC Particles on Vessel Formation and Stability in Vascularized Tissue Constructs. a) DPSCs and GFP-ECs were seeded into various hydrogel scaffolds to assess the effect of POMaC particles on vessel formation: GelMA scaffolds with and without POMaC particles and fibrin hydrogel tissues with and without POMaC particles. **b)** Representative images of GFP-EC (green)/DPSC co-cultures seeded into 3D-printed GelMA scaffolds with (right) and without (left) POMaC particles (blue). Scale bar = 100 μm. **c)** Quantification of vessel width in the tissues presented in b. Data are represented as mean ± SD, analyzed using an unpaired two-tailed *t*-test, *P < 0.05. **d)** Representative live imaging of GFP-EC (green)/DPSC in fibrin tissue constructs with and without POMaC particles (blue), taken on days 3, 6, 13, and 16 of culture. Scale bar = 100 μm. **e)** Measurement of green pixel density along the diagonal axis of each image. Data are represented as mean ± SD, n = 3 tissues, analyzed using two-way ANOVA with Bonferroni's post-test, **P < 0.01.

onto POMaC/GelMA 3D-printed constructs and monitored their development. The cells were cultured for 10 days, during which time they were allowed to spread and exhibit contractile activity (Fig. 5a). Troponin-T (TnT) staining indicated more robust cardiac tissue formation, which was further quantified using image analysis tools (Fig. 5b and ci). Cardiac function was also evaluated and showed improvement in constructs containing particles, as evidenced by a lower excitation threshold (Fig. 5cii) and an increased maximum capture rate (Fig. 5ciii). Additionally, the displacement amplitude was greater upon 1Hz stimulation in constructs with POMaC particles (Fig. 5civ and d and Video S10-11).

2.6. POMaC particles enhance in vitro vasculature stabilization in composite constructs

Vasculature formation is the key to the success of tissue engineering strategies. To this end, we seeded endothelial cells together with the supporting cells, dental pulp stem cells (DPSC), into two different matrices that incorporated the elastomeric POMaC particles: GelMA and fibrin (Fig. 6a). Vasculature formation within the GelMA/POMaC particle constructs was enhanced, with a significantly wider vessel diameter (Fig. 6b and c).

Next, we employed 3D printing of a mushroom-shaped structure to illustrate how a fibrin/POMaC particle hybrid bioink could influence vessel formation within 3D printed constructs. The stem of the mushroom, composed solely of cells and fibrin, contrasted with the cap, which contained the same components but also included POMaC particles. This resulted in distinct vessel formation types: the stem region, printed without particles, exhibited a non-organized, dense vasculature, whereas the vessels in the cap were elongated and utilized the particles as anchoring points (Figure S10).

Assessments of the temporal evolution of vessel formation from endothelial cells (ECs) and supporting cells within fibrin hydrogel constructs demonstrated enhanced stability in POMaC particle composite hydrogels, as evidenced by live imaging (Fig. 6d). Furthermore, blood vessels appeared to wrap around the POMaC particles, using them as anchoring points for stabilization (Fig. 6d).

To quantify vessel distribution throughout the tissue, we measured GFP intensity along two diagonal lines across the images. Our findings indicated no statistical difference in GFP intensities at earlier time points, with initial trends even favoring constructs without particles. However, this trend reversed at later time points, becoming significant on day 16 of culture and reflecting the increased vessel stability that occurs in the presence of POMaC particles (Fig. 6e).

To assess the organizational features of the particles within the tissues, we tracked particle displacements during the culture period by tracking the movement of autofluorescent particles within the EC/DPSC fibrin tissues over time (Figure S11a). Representative fluorescent images were captured on days 6, 9, 13, and 16, showing the particle distribution within the tissue matrix. By selecting a consistent reference particle (Figure S11b), we traced the relative displacement of neighboring particles throughout the culture period. The data were further analyzed to present both the magnitude and angular changes in particle displacement vectors across different time points. We noticed that over time, the magnitude of the displacement increased (Figure S11c), which we hypothesize is due to the matrix remodeling and degradation that occurs as the culture progresses. This degradation likely reduces the mechanical constraints within the matrix, allowing particles to move more freely. Interestingly, while the movement was stochastic at the earlier time points, it became more directional at the later stages of culture, likely due to the compression of the scaffold towards the center with higher tractional forces.

2.7. POMaC particles enhance angiogenesis and pro-regenerative macrophage recruitment in the composite constructs

To further investigate the long-term stability, structural integrity and functionality of the hydrogel scaffolds, we extended our in vivo studies from the initial 10-day period to 2 and 4 weeks. Gross morphology images of the explants at week 2 revealed that scaffolds containing particles exhibited a smaller scaffold area compared to the group without particles (Fig. 7a and b). We hypothesize that this is due to enhanced cell infiltration and subsequent material degradation, which is more pronounced in the presence of particles. Clear evidence of this is demonstrated in the group containing both particles and seeded cells (ECs/DPSCs), which exhibited increased vascularization within the implant on gross morphology (Fig. 7a). Notably, while all scaffolds appeared intact upon explanation, histological analysis revealed scaffold destabilization in the absence of particles, with significant shearing and tears observed in particle-free scaffolds as a result of histological processing (Fig. 7c and d and Figure S12a and b) and a larger amount of hydrogel remaining in the groups without particles (Figure S12b).

We further demonstrated a significant increase in blood vessel penetration in the groups containing POMaC particles, as quantified by CD31-positive staining (Fig. 8a and band Figure S13a). Additionally, we investigated macrophage infiltration into the implant and observed a significant increase in 4-week explants, as indicated by staining for both CD68 (a marker of total macrophages) and CD206 (a marker of pro-regenerative, pro-angiogenic macrophages infiltrating the tissue) (Fig. 8c–f and Figure S13b and c). These findings underscore the critical role of POMaC particles not only in enhancing vascularization and pro-regenerative macrophage infiltration but also in maintaining the structural integrity of the scaffolds, thereby supporting tissue integration and regeneration in vivo over an extended period.

3. Discussion

3D printing provides sophisticated structures for tissue and organ-on-a-chip engineering. However, extensive cellular tractional forces exert compression, generally resulting in the distortion of printed structures with time in culture or upon implantation [14,34] and eliminating the benefit of the original 3D printing process. It is critical to develop an approach that enables the maintenance of the 3D printed tissue shape during the tissue remodeling process in an environment that provides mechanical properties akin to that of native tissues [35]. Our work reveals that the incorporation of elastomeric POMaC particles into hydrogels generates a composite ink that both augments the mechanical robustness of the biofabricated tissues and also enhances cellular functionality in two examples, cardiac tissue engineering and vascularization.

We utilized two different methods for producing POMaC particles, bulk production and droplet microfluidics utilizing a PDMS device. The bulk generation approach is simple, inexpensive, and requires little equipment. It enables the production of a high number of particles in a short time period. However, the particle size distribution variability could be higher. Furthermore, the inability to regulate particle size and generation rate precisely may limit the use of bulk generation for studies that require uniform particle sizes or specified particle production rates. The microfluidic approach, on the other hand, provides a more controlled and accurate method for creating POMaC particles. The capability to meticulously regulate particle size and generation rates in microfluidics is instrumental in producing monodisperse particles. This level of control is especially beneficial in applications where particle size uniformity is critical.

Evaluating the efficacy of 3D printed structures extends beyond assessing the initial printability and immediate outcome post-bioprinting. It is imperative to consider the preservation of the construct's fidelity during the maturation phase. Frequently, the geometric and structural integrity of cell-laden constructs deteriorates over time
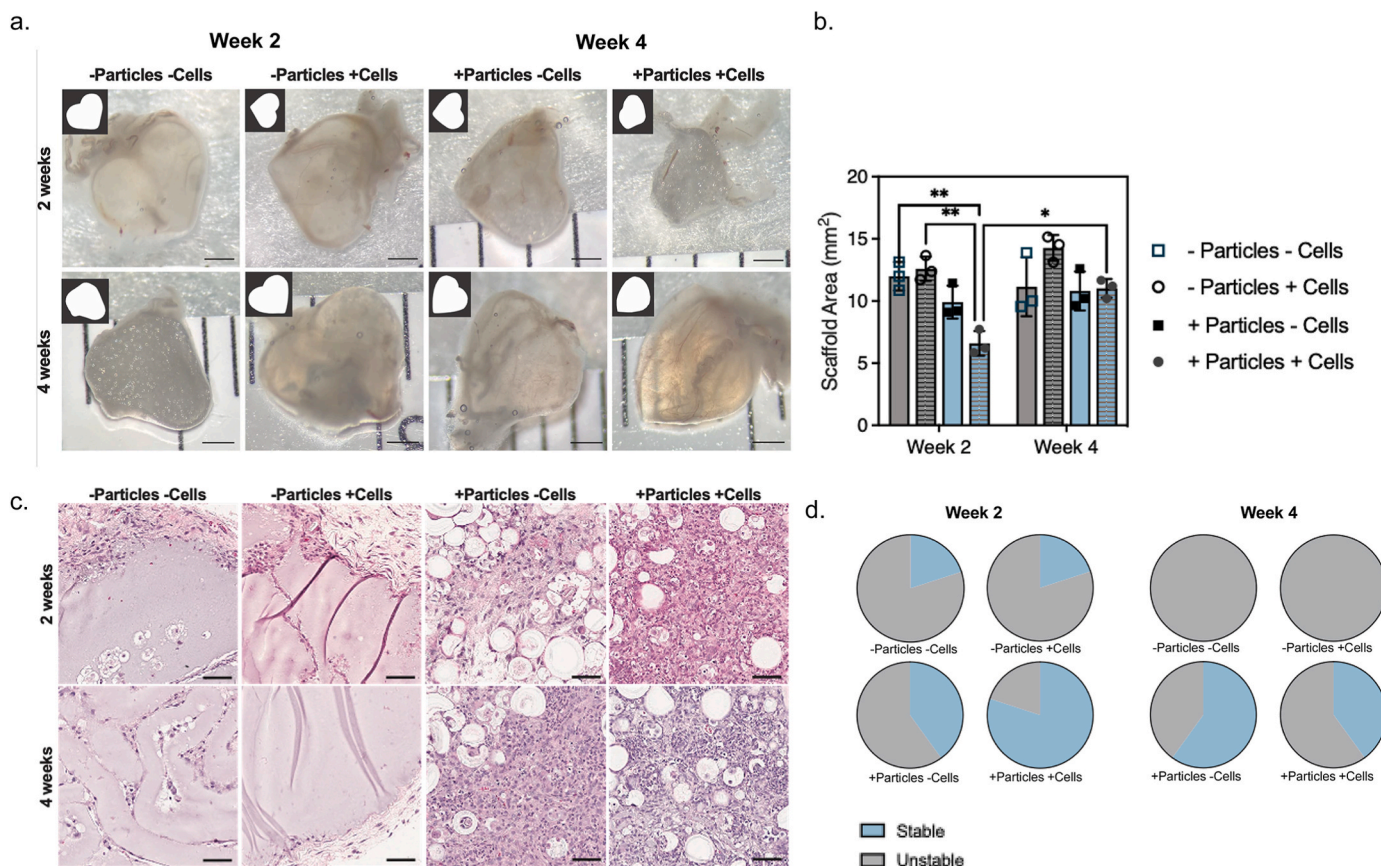
Fig. 7. Long-term *in vivo* implantation of POMaC particles/GelMA implants with and without cells. a) Representative images of scaffold gross morphology directly following explantation at 2 weeks and 4 weeks. Image masks used for area quantification are shown in the upper left corner for each scaffold. Scale bar 1 mm. **b)** Scaffold area at 2 weeks and 4 weeks post-implantation as quantified from gross morphology images. Data are represented as mean $\pm$ SD, n = 3 tissues, analyzed using two-way ANOVA with Bonferroni's post-test, *P < 0.05, **P < 0.01. **c)** Representative H&E histology images of scaffolds 2 and 4 weeks post-implantation. POMaC particles are seen as circular void spaces. Scale bar 50 μm. **d)** Quantification of scaffold stability from H&E images for samples explanted after 2 and 4 weeks. Scaffolds able to preserve their shape on histological sections were classified as stable, while those showing evidence of tearing and/or shearing were deemed unstable. Seeded cells include a co-culture of ECs and DPSCs.

due to hydrogel compaction, potentially leading to excessively high cell densities. This can compromise cell viability and impede proper cellular functions, as the encapsulated cells require a conducive environment to synthesize ECM components and facilitate tissue development and maturation [15,36]. Additionally, dimensional stability is paramount for constructs designated for implantation, where any shrinkage could result in misalignment with the target implantation site. Here, we demonstrated that the incorporation of particles into fibrin can modulate the degree of compaction rate. The biocompatibility, biological activity, and permeabilities of the hydrogel are maintained in the approach, enabling cellular functions. Yet, upon compression and cell remodeling, the particles are brought into closer contact, pushing against one another due to the elastomeric properties of the material, which then enables the construct to resist compression. We demonstrated that this approach can stabilize vascular networks over a prolonged period, a key requirement for successful tissue engineering.

Recent advances in the reinforcement of 3D bioprinted constructs have led to the development of innovative support strategies. One such strategy involves the utilization of a gel bath designed to support tissue culture by providing a stabilizing matrix [37]. Another approach entails the fabrication of a polymeric scaffold using poly(L-lactic acid)-poly (glycolic acid) (PLLA-PLGA) through molding printing, followed by the bioprinting of a hydrogel matrix with embedded cells around the scaffold [14]. However, these methodologies are inherently restricted to extrusion-based bioprinting processes, limiting their applicability across different bioprinting technologies. Our method is not restricted to a

specific printing technique. We demonstrated this by both stereolithography and extrusion-based printing. For stereolithography, we have shown that the integration of particles in the hydrogel bioink maintains the intricate architectural characteristics of this technique; in extrusion-based printing, our approach offered spatial control over the 3D construct, allowing selective elastomeric particle incorporation, which resulted in varying degrees of compaction within different regions of the structure over time.

One of the most significant challenges lies in maintaining both cell viability and structural stability for future implantation. Typically, there is a counter-directional trend: the less crosslinked the printed bioink encapsulating the cells, the more likely the cells are to thrive, proliferate, migrate, and secrete extracellular matrix (ECM). Conversely, a softer structure, while promoting these cellular activities, often results in poorer shape fidelity [15]. Incorporating POMaC particles into the composite bioinks had a substantial effect on the mechanical properties of the overall printed structure without changing the chemical properties of the hydrogel substrate with which the cells are in direct contact. These particles served as reinforcements for a variety of hydrogels, effectively distributing stress throughout the structure, reducing deformation, and increasing stability while simultaneously rendering the structure less brittle. This aspect holds critical significance in the realms of biological tissues and their manipulation upon *in vivo* implantation.

SEM imaging showed that constructs with POMaC particles are rougher, aligning with prior studies [38]. A key question emerging from our study is whether the observed effects on cellular behaviour and
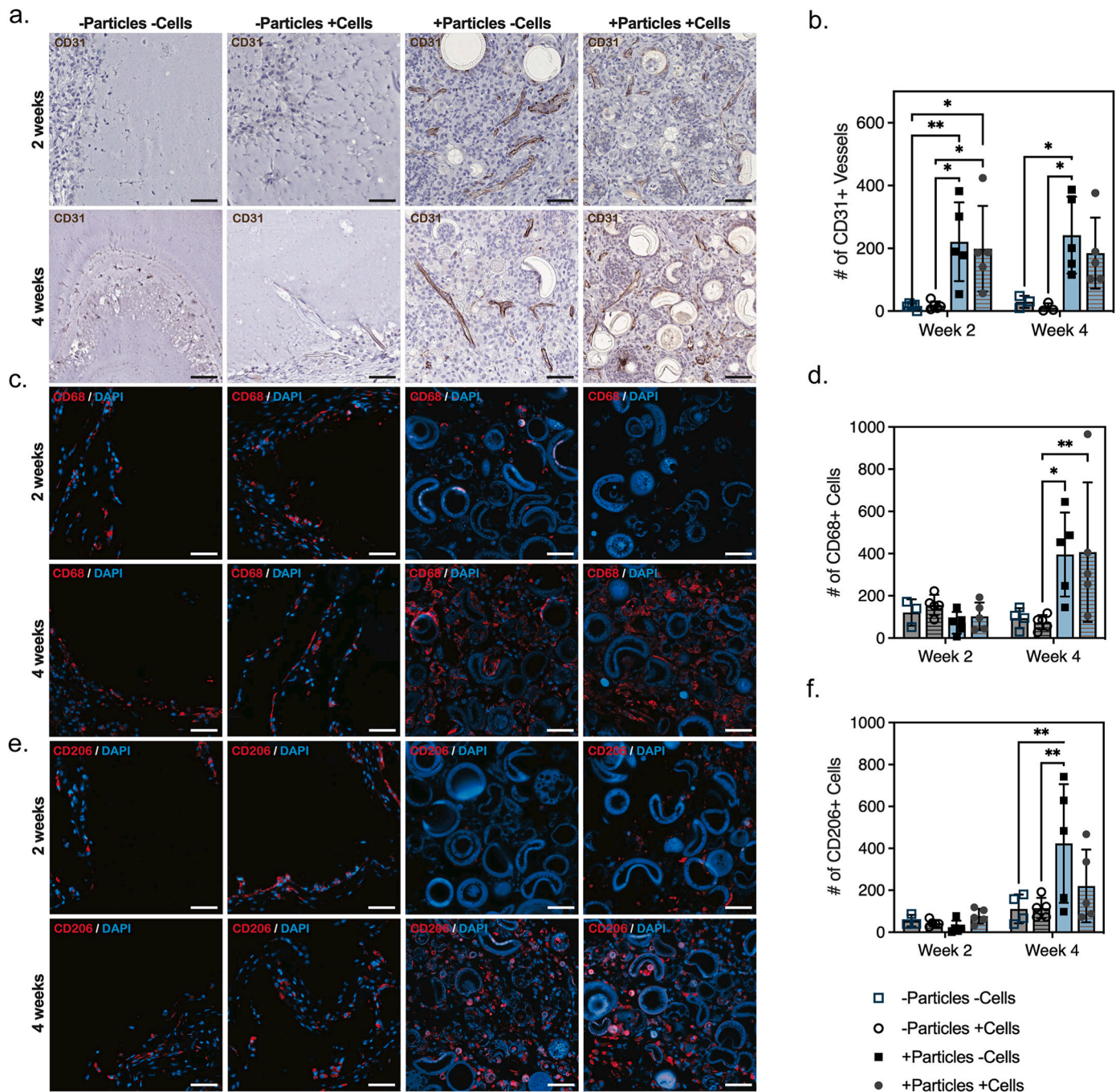
Fig. 8. The incorporation of POMaC particles into GelMA constructs induces blood vessel formation and pro-regenerative macrophage infiltration within the implants. **a)** Representative images of CD31 immunohistochemical staining of GelMA scaffolds with and without POMaC particles and cells following explantation at 2 weeks and 4 weeks. Scale bar = 50 μm. **b)** Quantification of blood vessels at 2 and 4 weeks post-implantation from immunohistochemistry images. Data are presented as mean ± SD, n = 5 tissues, and analyzed using two-way ANOVA with Tukey's post-test, $*P < 0.05$, $**P < 0.01$. **c)** Representative images of CD68 (red) and DAPI (blue) immunofluorescence staining of GelMA scaffolds with and without POMaC particles and cells following explantation at 2 weeks and 4 weeks. Scale bar = 50 μm. **d)** Quantification of CD68-positive cells at 2 and 4 weeks post-implantation from immunofluorescence images. Data are presented as mean ± SD, n = 5 tissues, and analyzed using two-way ANOVA with Tukey's post-hoc test, $*P < 0.05$, $**P < 0.01$. **e)** Representative images of CD206 (red) and DAPI (blue) immunofluorescence staining of GelMA scaffolds with and without POMaC particles and cells following explantation at 2 weeks and 4 weeks. Scale bar = 50 μm. **f)** Quantification of CD206-positive cells at 2 and 4 weeks post-implantation from immunofluorescence images. Data are presented as mean ± SD, n = 5 tissues, and analyzed using two-way ANOVA with Tukey's post-test, $*P < 0.05$, $**P < 0.01$. Seeded cells include a co-culture of ECs and DPSCs.

tissue integration are primarily driven by such structural differences introduced by the addition of particles or by the chemical composition of the particles. Our findings suggest that both factors may play important roles. We demonstrated that incorporating particles into the hydrogel increased surface roughness, which enhanced cell attachment, consistent with previous studies [39]. While surface topography can inhibit

cell proliferation, as noted in earlier studies [40], the chemistry of the constructs may also significantly influence tissue growth, particularly *in vivo*. This hypothesis is supported by our earlier work, where POMaC-based cardiac patches appeared to promote greater vascular infiltration and a reduced fibrotic response compared to other biomaterials [41]. In line with these findings, the current *in vivo* data

suggest that including particles in the scaffold may contribute to enhanced vascularization and increased infiltration of pro-angiogenic macrophages. While further studies are needed to fully elucidate the relative contributions of POMaC particles in terms of structural modifications and chemical properties, our results provide valuable insights that could inform the design of future biomaterials aimed at optimizing regenerative outcomes.

4. Conclusions

The results presented here are a promising avenue for the advancement of 3D bioprinting technologies, offering a balance between structural fidelity and biological function. The adaptability of the composite ink for various printing methods and hydrogels underscores the potential of the POMaC particle-hybrid bioink to cater to a variety of structural and functional requirements to advance applications in biomaterial science, tissue engineering, and regenerative medicine.

CRediT authorship contribution statement

Shira Landau: Writing – review & editing, Writing – original draft, Visualization, Validation, Software, Methodology, Investigation, Formal analysis, Data curation, Conceptualization. **Jennifer Kieda:** Writing – review & editing, Writing – original draft, Visualization, Validation, Software, Methodology, Investigation, Formal analysis, Data curation, Conceptualization. **Ramak Khosravi:** Writing – review & editing, Methodology, Formal analysis, Data curation. **Sargol Okhovatian:** Writing – review & editing, Writing – original draft, Visualization, Validation, Software, Methodology, Investigation, Formal analysis, Data curation, Conceptualization. **Kaitlyn Ramsay:** Writing – review & editing, Writing – original draft, Visualization, Validation, Software, Methodology, Investigation, Formal analysis, Data curation. **Chuan Liu:** Writing – review & editing, Methodology, Investigation, Data curation. **Amid Shakeri:** Writing – review & editing, Validation, Methodology, Investigation, Data curation, Conceptualization. **Yimu Zhao:** Data curation. **Karen Shen:** Data curation. **Orit Bar-Am:** Data curation. **Shulamit Levenberg:** Data curation. **Scott Tsai:** Writing – review & editing, Resources, Methodology, Conceptualization. **Milica Radisic:** Writing – review & editing, Writing – original draft, Visualization, Validation, Supervision, Resources, Project administration, Methodology, Investigation, Funding acquisition, Formal analysis, Data curation, Conceptualization.

Ethics approval and consent to participate

The animal study was done in the Technion and was approved by the Technion's inspection committee on the constitution of animal experimentation (assigned approval number: IL-0870619).

Declaration of competing interest

The authors declare the following financial interests/personal relationships which may be considered as potential competing interests: Milica Radisic reports financial support was provided by National Institutes of Health Grant 2R01 HL076485. Milica Radisic reports financial support was provided by Natural Sciences and Engineering Research Council of Canada (NSERC) Discovery Grant (RGPIN 326982-10). Milica Radisic reports financial support was provided by NSERC Strategic Grant (STPGP 506689-17). Milica Radisic reports financial support was provided by Canadian Institutes of Health Research (CIHR) Foundation Grant FDN-167274. Milica Radisic reports financial support was provided by Canada Research Chairs and Killam Fellowship. Shira Landau reports financial support was provided by Rothschild Fellowship. Shira Landau reports financial support was provided by EMBO ALTF 530–2022. If there are other authors, they declare that they have no known competing financial interests or personal relationships that could

have appeared to influence the work reported in this paper.

Materials and methods

POMaC synthesis

The POMaC synthesis process was built on the synthesis procedure that was previously published [42]synthesis procedure. POMaC synthesis began with the ratiometric addition of 1,8-octanediol (Sigma), maleic anhydride (Sigma), and 1,2,4-butanetricarboxylic acid (Sigma) into a 250 mL round-bottom flask where the reactive hydroxyl groups and carboxylic acid groups are balanced at 1:1. This ratio is critical to creating an optimized reaction with the chemically active sites fully reacting with each other. These reagents were melted at 160 °C and lowered to 140 °C at 200 rpm for 5 h. During this time, the entire reaction was kept under nitrogen purge to prevent unwanted side reactions due to oxidative species. The prepolymer was dissolved in 1,4-dioxane (Sigma) and collected in deionized distilled water. Once the reaction was complete, the deionized distilled water was decanted, and the prepolymer was purified. The final purified prepolymer solution was then dried in the fume hood with constant airflow for 48 h 5 wt% photoinitiator (2-hydroxy-1-[4(hydroxyethoxy)-phenyl]-2-methyl-1 propanone, Irgacure 2959, Sigma), as well as the porogen PEGDM (Sigma), was added at a ratio of 2:5 to the POMaC prepolymer. The prepolymer, porogen and photoinitiator are then mixed at 100 °C at 200 rpm for 15 min to create a homologous solution.

Manual compression tests

The manual compression experiments were carried out with a simple setup of two glass slides and a pair of tweezers. The glass slides were carefully cleaned to remove any impurities that would interfere with the compression process. The tweezers were chosen to provide precise control and allow for manual compression of the materials between the glass slides. Either a POMaC, PEG, or glass sample was placed on clean glass slides. To ensure consistent compression, the sample was positioned in the center of the slide. The second glass slide was then slowly lowered onto the sample using tweezers. Tweezers were used to apply gentle pressure on the top glass slide, compressing the material between the two slides.

NMR, FT-IR and Rheology

The viscosity of was measured by TA Instruments Discovery HR-2 rheometer equipped with a 40 mm 1.998° conical stainless-steel plate. More specifically, a flow sweep was performed at sheer rates from 0.1 1/s to 100 1/s (20 points, 25 °C), and an oscillation frequency was performed at a frequency of 0.1 Hz–50 Hz. (8 points, 25 °C). For FT-IR, samples were analyzed by ATR-FTIR on a PerkinElmer (Shelton, CT) Spectrum Two FTIR spectrometer.Compression testing for GelMA-3D printed structures with and without particles was done by compressing the construct until failure. The measured force was then divided by

the structure's cross-section. A stress-strain curve was then generated, and Young's modulus was calculated from the linear range of the curve.

POMaC Particles synthesis

The bulk method

Spherical particles were fabricated by infusing POMaC into a 1 w/v % polyvinyl alcohol (PVA) solution at 16 mL/h using a syringe pump (Fisherbrand™ 780100I). The 1 w/v % PVA solution was made by dissolving PVA (87–90 % hydrolysis degree, Sigma Aldrich) in Milli-Q water (1 wt%) and stirring at room temperature for approximately 40 min, or until fully dissolved. Particle shearing was achieved by stirring the PVA solution with a magnetic stir bar at 1000 rpm. Followed by crosslinking in a UV chamber (Analytik Jena US, MA, USA)) for 90 min of 18.9J/cm^2. The particles were then filtered with a cell strainer (40 μm – 70 μm, Corning™ Falcon™ Cell Strainers).

The microfluidic method

A conventional soft lithography approach was used to create microfluidic devices [43]. The microfluidic device for emulsion creation is a flow-focusing device with a single junction. It has two inlets: one for the dispersed phase and one for the continuous phase. The orifice of the device is 140 μm and the channel width is 150 μm with the device height being 210 μm. The channel width from the first junction to the outer is 300 μm.The dispersed phase consisted of the POMaC pre-polymer and the continuous phase consisted of mineral oil (Sigma-Aldrich) and 5 v/v % of Span-80 surfactant. All the flows were injected into the microfluidic device through Polyether ether ketone (PEEK) tubing (OD = 1/16 in., ID = 0.020 in.; IDEX Health and Science), using a microfluidic flow control system (FLOW EZ, Fluigent, Paris, France), and were controlled by a Microfluidic Automation Tool software (Fluigent, Paris, France). The pressure for the dispersed POMaC phase was set at 240 mbar and the pressure for the continuous mineral oil was set to 100 mbar. Experimental images and videos were captured using a high-speed camera (Miro M110, Vision Research, Wayne, NJ) connected to an inverted brightfield optical microscope (Axio Observer A1, Carl Zeiss, Oberkochen, Germany). Once droplets were formed, they exited the device outlet through PEEK tubing into a conventional Petri dish. Droplets were then stirred using a magnetic stir bar by a hot plate. In the Petri dish, a UV flashlight (Labino, Sweden) was shined over the droplets for 5 min where they were crosslinked.

Micromechanical testing

A CellScale MicroTester G2 (MT G2) was utilized to apply precise amounts of strain to the POMaC particles or GelMA heart structures. A tungsten 0.5588 mm O.D. microbeam provided by the manufacturer, with a 2 × 2 cm plate (thickness 51 μm), was glued to the end of the beam was attached to the MT G2 all provided by the manufacturer and was done according to the manufacturer's instructions. POMaC particles or GelMA or alginate printed structures were placed in an aqueous solution on top of a small metal block. The attached plate was then lowered such that the microbeam was slightly in contact with the sample. Repeated compress magnitude deformations of 10–20 % strain were applied for 3 cycles. Each cycle had a loading duration of 30 s, followed by a hold of 10 s, then a recovery duration of 30 s, and lastly, a rest duration of 10 s. The resulting output of these experiments included the displacement and the force at 1s intervals throughout the cyclic tests. This was then used to calculate stiffness by dividing the measured force by the beam size and calculating the strain.

Finite element modelling of stress distribution in composite structures

For the finite element modeling of stress distribution within the

GelMA construct, with and without particles, SimScale software was utilized. A box measuring 4×10^{-5} by 4×10^{-5} by 1.2×10^{-4} m was created to simulate the construct composed solely of GelMA. In the models representing the GelMA with POMaC particles, two spheres (each with a diameter of 4×10^{-5} m) were incorporated. Material properties were determined as follows: Young's modulus and the Poisson's ratio for POMaC particles and GelMA were calculated from microSquisher analysis, with the Poisson's ratio derived from micro-Squisher images. The density of POMaC was referenced from the literature [33], and the density of GelMA was calculated by dividing the mass by the volume. The boundary conditions applied were: 1) Fixed support at one end of the construct, and 2) An applied force of 1 μN at the other end.

Particle displacement analysis

To analyze the displacement of particles over time, 4 sequential images were acquired at different time points: Day 6, Day 9, Day 13, and Day 16. Each image was converted to grayscale for uniformity in analysis. Using custom MATLAB scripts, 20 particles were manually selected in each image, and a reference point was also designated to facilitate relative displacement calculations. For each selected particle, the displacement vectors between consecutive time points were calculated. The displacement vector for each particle between two-time points was computed and displayed.

Preparation of PEG particles

To fabricate polyethylene glycol (PEG) particles, PEG diacrylate (PEGDA, average Mn 250), was first mixed with 5 % vol/vol ratio of 2-Hydroxy-2-methylpropiophenone as a photoinitiator. This mixture was then incrementally added to a continuously stirred polyvinyl alcohol (PVA) solution at a speed of 1000 rpm, utilizing a syringe fitted with a G23 needle for the dropwise addition. Subsequently, the blend was subjected to UV light exposure using a UV flashlight (UVG3 Floodlight, Labino), producing energy of 12–45 mW/cm^2, for a period of 20 min while maintaining stirring to ensure even polymerization and particle formation. Following this, the polymerized particles were separated from the mixture through filtration using a 100 μm cell strainer, yielding the final PEG particles.

PEG and glass constructs

Glass particles (Sigma-Aldrich, 75 μm) or PEG particles were mixed with GelMA in a 50:50 particle-to-gel ratio. 70 μl of the mixture was dispensed onto a Petri dish and exposed to UV light using a UV flashlight (UVG3 Floodlight, Labino) producing and energy of 12–45 mW/cm^2 for 30 min on each side. Subsequently, the samples were photographed to measure cross-sectional dimensions and were subjected to compression testing.

Cell Culture and Differentiation

Human Umbilical Vein Endothelial Cells (HUVECs. cAP-0001GFP, Angioprotemie), were cultured in EGM2 medium (ScienceCell). Dental pulp stem cells (DPSC, PT-5025, Lonza) were cultured in a low-glucose DMEM, enriched with 10 % Fetal Bovine Serum (FBS), 1 % Non-Essential Amino Acids (NEAA), 1 % GlutaMAX™, and 1 % penicillin-streptomycin, with media change every two days. Human cardiac fibroblasts (PromoCell) were cultured in fibroblasts growth medium 3 (PromoCell).

Cardiac differentiation of BJ1D induced Pluripotent Stem Cells (iPSCs) was routinely carried out in six-well plates coated with Matrigel, employing mTeSR™ Plus medium. The differentiation protocol followed a previously established method, starting with the iPSCs seeded in 12-well plates at a density of 0.75 million cells per well. Cells were

maintained in mTeSR™ Plus medium until they reached full confluence within 24–48 h. At that point, RPMI medium supplemented with B27 minus insulin, penicillin-streptomycin, and 8 μM CHIR99021 was introduced on day zero. CHIR99021 was removed after a 24-h period, and 5 μM IWP4 was added on day three, which was then removed after an additional 48 h. From day seven onwards, the culture was maintained in RPMI supplemented with B27 minus insulin, and later transitioned to RPMI with B27. Cardiomyocytes were dissociated using 10X TrypLE™ Express for 15–30 min at 37 °C.

For GFP tagged HES2 ventricular cardiomyocyte differentiation, a modified version of the embryoid body (EB)-based protocol described in Ref. [44] was followed. hPSC populations (HES2) were dissociated into single cells (TrypLE, ThermoFisher) and re-aggregated to form EBs in StemPro-34 media (ThermoFisher) containing penicillin/streptomycin (1 %, ThermoFisher), L-glutamine (2 mM, ThermoFisher), transferrin (150 mg/ml, ROCHE), ascorbic acid (50 mg/ml, Sigma), and mono-thioglycerol (50 mg/ml, Sigma), ROCK inhibitor Y-27632 (10 μM, TOCRIS) and rhBMP4 (1 ng/ml, R&D) for 18h on an orbital shaker (70 rpm). On day 1, the EBs were transferred to mesoderm induction media consisting of StemPro-34 with the above supplements, excluding ROCK inhibitor Y-27632 and rhBMP4 (12 ng/ml), rhActivinA (8 ng/ml, R&D) and rhbFGF (5 ng/ml, R&D). On day 3, the EBs were harvested, dissociated into single cells (TrypLE), and re-aggregated in cardiac mesoderm specification media consisting of StemPro-34, the Wnt inhibitor IWP2 (2 μM, TOCRIS) and rhVEGF (10 ng/mL, R&D). On day 5, the EBs were transferred to StemPro-34 with rhVEGF (5 ng/ml) for another five days and then to StemPro-34 media (ThermoFisher) containing penicillin/streptomycin (1 %, ThermoFisher), L-glutamine (2 mM, ThermoFisher), transferrin (150 mg/ml, ROCHE), ascorbic acid (50 mg/ml, Sigma), and monothioglycerol (50 mg/ml, Sigma) for another 10 days. Cultures were incubated in a low oxygen environment (5 % CO_2, 5 % O_2, 90 % N_2) for the first ten days and a normoxic environment (5 % CO_2, 20 % O_2) for the following 10 days.

Fibrin hydrogel tissues

To create vascularized fibrin tissues, HUVEC and DPSC were mixed at a 1:1 ratio in the concentration of 1.6M cells/ml. Cells were resuspended in bovine fibrinogen (40 mg/ml, Sigma-Aldrich) with and without POMaC particles (2million/ml) followed by mixing the fibrinogen/cells mixture with Thrombin (4U/ml, Sigma-Aldrich), at 1:1 ratio to mimic the 3D printing conditions. 20 μl of cell-fibrin mixture was immediately seeded on a suspension 6-well plate and incubated for 37 °C for 30min followed by EGM2 media addition.

For fibroblasts seeded in floating fibrin constructs, Pluronic acid treatment was done to prevent the fibrin attachment to the bottom of the plate post seeding. Cardiac fibroblasts were resuspended in human fibrinogen (33 mg/ml, Sigma-Aldrich) with and without POMaC particles (1M/ml) followed by mixing the fibrinogen/cells mixture with Thrombin (20U/ml, Sigma-Aldrich), at 2:7 ratio. A volume of 20 μl of the fibrin mixture were immediately seeded on a suspension 6-well plate and incubated for 37 °C for 30min followed by fibroblasts growth medium 3 (PromoCell) addition. Tissues' size was measured on days 0, 6, 8 and 11 of culture by bright field microscopy and Alamar blue assay (Thermo Fisher Scientific) was performed on day 3 and 8 of culture according to the manufacture's instruction.

Live/dead assay

To assess tissue viability, DPSCs (3.3M cells/ml fibrin) were seeded within fibrin hydrogel on a GelMa printed construct (with a 50:50 particles to GelMa ratio). Tissues were cultured for 7 days. On the 7th day, tissues were washed with PBS and then treated with propidium iodide (PI, 2.5 μg/mL, Life Technologies, P3566) and carboxyfluorescein diacetate-succinimidyl ester (CFDA-SE, 10 μM, Life Technologies, C1157) for 30 min at 37 °C, washed with media and imaged immediately.

3D printing

Stereolithography

For structures created using stereolithography technique, heart structures were first designed in Fusion360 (with major axis' dimensions of x-16mm, y-16mm, z-0.5 mm). These designs were then printed using a 3D printer (Lumen X+, CellInk). The bioink consisted of either GelMA PhotoInk (CellInk) or GelMA PhotoInk with added POMaC particles (50:50), or PEGDA with (50:50) and without POMaC particles. Hearts were then analyzed for stability, swelling, handling and auto-fluorescence. The printed structures were then γ-sterilized and placed in well plates. Differentiated cardiomyocytes were dissociated from their culturing dish and were seeded into the GelMA/POMaC heart constructs, and the control GelMA heart constructs with a seeding density of 50M cells/ml of 50:50 GFP tagged HES2 ventricular cardiomyocyte and iPSCs BJ1D cardiomyocytes. The seeded cell-heart structures were then incubated for 10 min followed by media addition that contains StemPro-34 complete media supplemented with 20 mM HEPES, 1 % GlutaMAX, and 213 μg/mL 2-phosphate ascorbic acid. Cardiac constructs were cultured for 10 days followed by electrical activity assessment and immunostaining. For vasculature seeded on GelMA constructs- EC/DPSC were mixed with a ratio of 1:1 and then seeded with a cell concentration of 13M cells/ml and cultured for 10 days with EGM2 (ScienceCell) media.

Extrusion printing

For structures created using extrusion printing, we used the Bio-AssemblyBot 400 to deposit bovine fibrinogen bioink (Sigma-Aldrich, 40 mg/ml in saline) mixed with Cells (HUVEC and DPSC, 1.6Mcells/ml) with and without POMaC particles (2M/ml) accurately and automatically into a FRESH (Freeform Reversible Embedding of Suspended Hydrogels, see preparation below) bath supplemented with Thrombin (Sigma-Aldrich, 12U/ml in saline). Within a controlled and sterile setting, the control software is utilized to import a three-dimensional representation of the desired tissue structure. The configuration of printing parameters, including speed, extrusion pressure, and layer thickness is determined according to the specific needs of the bioink and construct. The printing procedure is commenced, wherein the Bio-AssemblyBot 400 carries out pre-programmed motions to deposit successive layers of fibrinogen bioink into the FRESH solution. After printing, constructs EGM2 media was added to the well and constructs were incubated at 37 °C for about 1 h to melt the gelatin, followed by replacement of the melting gelatin with fresh media supplemented with Antibiotic-Antimycotic (1 %, Thermo Scientific).

FRESH bath preparation

Water and ethanol were combined in a 1L beaker with a large magnetic stir bar then 200 μl of 10M NaOH was added to the water: ethanol mixture. The mixture was then heated to 45 °C at 200 RPM. Then Gelatin Type-b from Bovine skin (Sigma-Aldrich, 20 g), Pluronic F-127 (Sigma-Aldrich,2.5 g) and Gum Arabia (Sigma-Aldrich,1 g) powders were added to the solution (powders were UV sterilized) and mixed for 10 min until fully dissolved. pH was then fixed to reach 6.25. The solution was then stirred at 150RPM over-night at room temperature. The mixture was then divided into 50 ml tubes and centrifuged at 500 RCF for 10min and twice at 1000RCF for 2 min. The solution was washed in between with a washing solution (20 mM Hepes, 10 % saline, and 1 % calcium in ddw). Bovine Thrombin (Sigma-Aldrich) at 12U/ml was added to the washing solution before printing.

Alginate tubes fabrication

The POMaC particle-embedded alginate tubes were fabricated using a custom-made coaxial microfluidic spinning device where 1 % alginate and 100 mM calcium chloride solution were extruded as the outer and inner flow, respectively. Before microfluidic spinning, POMaC particles were dispersed in the alginate solution and Alcian Blue was added to the alginate solution for visualization. The alginate and calcium chloride solutions were pumped through the microfluidic spinning device using two syringe pumps at a flow rate of 40 μl/min and 20 μl/min, respectively. Due to immediate crosslinking between alginate and calcium ions, a tube was formed when the alginate and calcium chloride inside the coaxial channel were pumped into a calcium chloride bath where a long particle-embedded alginate tube was collected.

Tissue morphology evaluation

Fluorescent microscopy

Tissues in fibrin gels and 3D printed constructs were observed under the fluorescence microscope (Olympus IX81) every 2–3 days and images were taken to evaluate the vascular formation within the tissues and the overall tissue construct integrity. The location and morphology of HUVECS (GFP-Green) and POMaC particles were monitored to understand the dynamic nature of the formed tissues over time.

SEM

Sample characterization of POMaC particles generated using the bulk and microfluidic approach and GelMA 3D printed constructs with and without POMaC particles, was done in a Hitachi SU 3500 VPSEM, using high vacuum mode. An electron beam voltage of 1.5 kV was used as well as a large working distance of approximately 31 mm–32 mm. Samples were characterized without any conductive sputter coating applied.

Printability Assessment

To evaluate printability, we fabricate various heart-shaped PEGDA constructs using the Lumen X+ 3D printer. We varied particle sizes (both larger and smaller than 100 μm) and particle concentrations (20 %, 50 %, and 70 %) mixed with PEGDA. Immediately following the printing process, the constructs were imaged and subsequently compared to the original print design using a custom MATLAB script. Briefly, the images were converted to binary format and analyzed for shape fidelity using the Procrustes function from the Statistics and Machine Learning Toolbox. This function quantifies dissimilarity between shapes through Procrustes analysis by determining the optimal shape-preserving Euclidean transformation, which encompasses rotation, reflection, scaling, and translation. In this context, the Procrustes transformation was applied to compare the original design (shape X) with the printed construct (shape Y), thereby providing a precise measure of print fidelity.

Force characterization of cardiac tissues

Assessment of force in the cardiac constructs was performed according to established protocols [45]. In summary, 10 days post-seeding, tissues were transferred to an electric stimulation chamber, which was interfaced with a Grass ×88 stimulator for functional analysis, where we determined the excitation threshold (ET at 1Hz) along with the highest capture rate (at twice the ET value). Beating amplitude during 1Hz electrical stimulation was measured by a video capturing tissue contraction and processed using an established MATLAB algorithm.

Immunofluorescence staining and confocal imaging

On day 10 of culturing cardiac tissues were fixed with 4 % PFA for 20 min at RT, permeabilized using 0.3 % Triton for 20 min and blocked using 5 % BSA in PBS for 2 h before adding the primary antibodies. All staining incubation was performed at 4C. Mouse-anti-Troponin-T (1:200, Invitrogen, MA512960, lot# 2417682) was applied for 24 h, followed by 3 PBS washes, each for 10 min, followed by 24 h of secondary antibody incubation with Alexa Fluor TM 647 goat anti-mouse IgG1 (1:400, Invitrogen A21240, lot #2185066) as secondary antibody. The nuclei were with DAPI (1:1000, Invitrogen, D1306, lot# 2274788) for the nucleus. The tissues were imaged with a Leica light-sheet confocal microscope at 10x and 20× magnifications.

Subcutaneous Implantation

For the day 10 time point, the cell-free scaffolds were implanted at Technion Israel Institute of Technology according to the protocol approved by the Technion's inspection committee on the constitution of animal experimentation (assigned approval number: IL-0870619). Athymic nude mice (male, 7 weeks old; Harlan Laboratories) were anesthetized with isofluorane. Heart-shaped scaffolds with and without POMaC particles were subcutaneously implanted on the back of 5 Nude mice. In each mouse, 4 scaffolds, 2 of each type, were implanted in the same 4 positions, whereas the order of the scaffold types was changed in each animal. Ten days post-implantation, mice were intravenously injected with 100 μl of TRITC-Dextran (10 mg/ml, Sigma-Aldrich), anesthetized with isofluorane, and sacrificed about 10–15 min later with CO2. The scaffolds were exposed, removed, and imaged by a digital camera and a confocal microscope (Zeiss LSM 700).

For evaluation of cell-seeded constructs, upon longer 2 and 4 week implantation, adult male (n = 5) and female (n = 5) athymic mice (age 7–8 weeks, Charles River Laboratories) were used for *in vivo* studies according to protocol #20012969) approved by the University of Toronto Animal Care Committee. Following induction of anesthesia with isoflurane, four 1 cm dorsal incisions were made on the back of each mouse and heart-shaped scaffolds were subcutaneously implanted in each associated region. Each animal received four variants of GelMA scaffolds: with and without POMaC particles, and with and without seeded GFP-HUVECS and DPSCs. At 2 and 4 weeks post-implantation, mice were euthanized and the scaffolds exposed and gently dissected from the surrounding subcutaneous tissue. Samples were then removed for imaging and histological/immunohistochemical studies.

Histology and Immunohistochemistry for In Vivo Samples

Scaffolds explanted at 2 weeks and 4 weeks were imaged under a dissecting microscope for quantification of scaffold area and subsequently placed within a 10 % neutral buffered formalin solution overnight. Samples were then embedded in paraffin, sectioned serially (4 μm thickness), and stained with hematoxylin and eosin (H&E). Scaffold stability was quantified as the absence of obvious shearing and/or tearing of the scaffold on H&E histological sections. For immunofluorescence staining, 4 μm thick sections were deparaffinized and rehydrated prior to heat-mediated antigen retrieval in citrate buffer for 25 min. Following blocking with Protein Block (Aligent Dako) to reduce nonspecific background staining, sections were incubated overnight with antibodies for CD68 (Abcam ab125212, 1:500) or CD206 (Abcam ab64693, 1:500). Primary antibody binding was visualized using species-specific Alexa Fluor 488 and 647–conjugated secondary antibodies (Thermo Fischer Scientific). Sections were counterstained with DAPI (1:1000, Thermo Fischer Scientific) and mounted using Fluorescence Mounting Medium (Aligent Dako). For immunohistochemical staining, slides were deparaffinized and heat-mediated antigen retrieval performed in the same manner. Endogenous peroxidase activity was quenched via incubation with 3 % hydrogen peroxide. Following

blocking with 2.5 % normal horse serum, sections were incubated overnight with primary antibodies for CD31 (Novus NB-100-2284, 1:300). Slides were developed using the ImmPRESS® HRP Horse Anti-Rabbit IgG Polymer Detection Kit (Vector Laboratories MP-7401) following the manufacturer's protocol, followed by color development with DAB (Dako). Sections were counterstained with hematoxylin and mounted using MM23 mounting media (Leica).

Fluorescence images were digitally acquired with a Zeiss AxioObserver microscope attached to a Hamamatsu ORCA-Flash 4.0 camera under a 20× magnification objective. Brightfield images were acquired using the Aperio AT2 brightfield scanner (Leica Biosystems) at 20× magnification. Image analysis was performed using ImageJ (CD31 images) or a custom MATLAB script (CD68 and CD206 images).

Statistical analysis

Statistical analysis was performed using Prism 10. Differences between experimental groups were analyzed by one-way ANOVA (more than two groups), two-way ANOVA, or *t*-test (among two groups). Statistical significance was set at $p < 0.05$ and indicated in figures as * $p < 0.05$, **$p < 0.01$, ***$p < 0.001$, ****$p < 0.0001$.

Appendix A. Supplementary data

Supplementary data to this article can be found online at https://doi.org/10.1016/j.bioactmat.2024.10.008.

Data availability

Raw data for this paper can be found in Landau, Shira (2024), "Cell driven elastomeric particle packing in composite bioinks for engineering and implantation of stable 3D printed structures", Mendeley Data, V1, doi: 10.17632/kdkpfpktw5.1

References

[1] S.V. Murphy, A. Atala, 3D bioprinting of tissues and organs, Nat. Biotechnol. 32 (2014) 773–785.
[2] D. Huang, Y. Huang, Y. Xiao, X. Yang, H. Lin, G. Feng, X. Zhu, X. Zhang, Viscoelasticity in natural tissues and engineered scaffolds for tissue reconstruction, Acta Biomater. 97 (2019) 74–92.
[3] S.M. Hull, L.G. Brunel, S.C. Heilshorn, 3D bioprinting of cell-laden hydrogels for improved biological functionality, Adv. Mater. 34 (2022) 2103691.
[4] B.A. de Melo, Y.A. Jodat, E.M. Cruz, J.C. Benincasa, S.R. Shin, M.A. Porcionatto, Strategies to use fibrinogen as bioink for 3D bioprinting fibrin-based soft and hard tissues, Acta Biomater. 117 (2020) 60–76.
[5] J. Yin, M. Yan, Y. Wang, J. Fu, H. Suo, 3D bioprinting of low-concentration cell-laden gelatin methacrylate (GelMA) bioinks with a two-step cross-linking strategy, ACS Appl. Mater. Interfaces 10 (2018) 6849–6857.
[6] W. Kim, G. Kim, 3D bioprinting of functional cell-laden bioinks and its application for cell-alignment and maturation, Appl. Mater. Today 19 (2020) 100588.
[7] J. Stepanovska, M. Supova, K. Hanzalek, A. Broz, R. Matejka, Collagen bioinks for bioprinting: a systematic review of hydrogel properties, bioprinting parameters, protocols, and bioprinted structure characteristics, Biomedicines 9 (2021) 1137.
[8] P.S. Gungor-Ozkerim, I. Inci, Y.S. Zhang, A. Khademhosseini, M.R. Dokmeci, Bioinks for 3D bioprinting: an overview, Biomater. Sci. 6 (2018) 915–946.
[9] D. Rana, P. Padmanaban, M. Becker, F. Stein, J. Leijten, B. Koopman, J. Rouwkema, Spatial control of self-organizing vascular networks with programmable aptamer-tethered growth factor photopatterning, Mater. Today Biol. 19 (2023) 100551.
[10] N. Alemdar, J. Leijten, G. Camci-Unal, J. Hjortnaes, J. Ribas, A. Paul, P. Mostafalu, A.K. Gaharwar, Y. Qiu, S. Sonkusale, Oxygen-generating photo-cross-linkable hydrogels support cardiac progenitor cell survival by reducing hypoxia-induced necrosis, ACS Biomater. Sci. Eng. 3 (2017) 1964–1971.
[11] A. Mostafavi, M. Samandari, M. Karvar, M. Ghovvati, Y. Endo, I. Sinha, N. Annabi, A. Tamayol, Colloidal multiscale porous adhesive (bio) inks facilitate scaffold integration, Appl. Phys. Rev. 8 (2021).
[12] K. Nuutila, M. Samandari, Y. Endo, Y. Zhang, J. Quint, T.A. Schmidt, A. Tamayol, I. Sinha, In vivo printing of growth factor-eluting adhesive scaffolds improves wound healing, Bioact. Mater. 8 (2022) 296–308.
[13] R.P. Accolla, M. Deller, T.R. Lansberry, A. Simmons, J.-P. Liang, S.N. Patel, K. Jiang, C.L. Stabler, 3D printed elastomeric biomaterial mitigates compaction during in vitro vasculogenesis, Acta Biomater. 171 (2023) 363–377.
[14] A.A. Szklanny, M. Machour, I. Redenski, V. Chochola, I. Goldfracht, B. Kaplan, M. Epshtein, H. Simaan Yameen, U. Merdler, A. Feinberg, 3D bioprinting of
engineered tissue flaps with hierarchical vessel networks (VesselNet) for direct host-to-implant perfusion, Adv. Mater. 33 (2021) 2102661.
[15] R. Levato, T. Jungst, R.G. Scheuring, T. Blunk, J. Groll, J. Malda, From shape to function: the next step in bioprinting, Adv. Mater. 32 (2020) 1906423.
[16] S. Tortorella, P. Greco, F. Valle, M. Barbalinardo, G. Foschi, F. Lugli, M. Dallavalle, F. Zerbetto, C.A. Bortolotti, F. Biscarini, Laser Assisted Bioprinting of laminin on biodegradable PLGA substrates: effect on neural stem cell adhesion and differentiation, Bioprinting 26 (2022) e00194.
[17] R. Khoeini, H. Nosrati, A. Akbarzadeh, A. Eftekhari, T. Kavetskyy, R. Khalilov, E. Ahmadian, A. Nasibova, P. Datta, L. Roshangar, Natural and synthetic bioinks for 3D bioprinting, Adv. NanoBiomed. Res. 1 (2021) 2000097.
[18] P.A. Gunatillake, R. Adhikari, N. Gadegaard, Biodegradable synthetic polymers for tissue engineering, Eur. Cell. Mater. 5 (2003) 1–16.
[19] C.F. Guimarães, L. Gasperini, A.P. Marques, R.L. Reis, The stiffness of living tissues and its implications for tissue engineering, Nat. Rev. Mater. 5 (2020) 351–370.
[20] L.D. Huyer, M. Montgomery, Y. Zhao, Y. Xiao, G. Conant, A. Korolj, M. Radisic, Biomaterial based cardiac tissue engineering and its applications, Biomed. Mater. 10 (2015) 034004.
[21] S. Okhovatian, A. Shakeri, L. Davenport Huyer, M. Radisic, Elastomeric polyesters in cardiovascular tissue engineering and organs-on-a-chip, Biomacromolecules 24 (2023) 4511–4531.
[22] B. Zhang, M. Montgomery, M.D. Chamberlain, S. Ogawa, A. Korolj, A. Pahnke, L. A. Wells, S. Massé, J. Kim, L. Reis, Biodegradable scaffold with built-in vasculature for organ-on-a-chip engineering and direct surgical anastomosis, Nat. Mater. 15 (2016) 669–678.
[23] H. Savoji, L. Davenport Huyer, M.H. Mohammadi, B.F. Lun Lai, N. Rafatian, D. Bannerman, M. Shoaib, E.R. Bobicki, A. Ramachandran, M. Radisic, 3D printing of vascular tubes using bioelastomer prepolymers by freeform reversible embedding, ACS Biomater. Sci. Eng. 6 (2020) 1333–1343.
[24] C. Liu, S.B. Campbell, J. Li, D. Bannerman, S. Pascual-Gil, J. Kieda, Q. Wu, P. R. Herman, M. Radisic, High throughput omnidirectional printing of tubular microstructures from elastomeric polymers, Adv. Healthcare Mater. 11 (2022) 2201346.
[25] V. Karamzadeh, M. Shen, H. Ravanbakhsh, A.S. Kashani, H. Savoji, M. Radisic, D. Juncker, High-resolution additive manufacturing of a biodegradable elastomer with a low-cost LCD 3D printer, Adv. Healthcare Mater. 13 (2023) 2303708.
[26] A. Ribeiro, M.M. Blokzijl, R. Levato, C.W. Visser, M. Castilho, W.E. Hennink, T. Vermonden, J. Malda, Assessing bioink shape fidelity to aid material development in 3D bioprinting, Biofabrication 10 (2017) 014102.
[27] L. Davenport Huyer, A.D. Bannerman, Y. Wang, H. Savoji, E.J. Knee-Walden, A. Brissenden, B. Yee, M. Shoaib, E. Bobicki, B.G. Amsden, One-pot synthesis of unsaturated polyester bioelastomer with controllable material curing for microscale designs, Adv. Healthcare Mater. 8 (2019) 1900245.
[28] G. Choe, M. Lee, S. Oh, J.M. Seok, J. Kim, S. Im, S.A. Park, J.Y. Lee, Three-dimensional bioprinting of mesenchymal stem cells using an osteoinductive bioink containing alginate and BMP-2-loaded PLGA nanoparticles for bone tissue engineering, Biomater. Adv. 136 (2022) 212789.
[29] C.M. Boutry, Y. Kaizawa, B.C. Schroeder, A. Chortos, A. Legrand, Z. Wang, J. Chang, P. Fox, Z. Bao, A stretchable and biodegradable strain and pressure sensor for orthopaedic application, Nat. Electron. 1 (2018) 314–321.
[30] B. Zhang, M. Montgomery, M.D. Chamberlain, S. Ogawa, A. Korolj, A. Pahnke, L. A. Wells, S. Masse, J. Kim, L. Reis, A. Momen, S.S. Nunes, A.R. Wheeler, K. Nanthakumar, G. Keller, M.V. Sefton, M. Radisic, Biodegradable scaffold with built-in vasculature for organ-on-a-chip engineering and direct surgical anastomosis, Nat. Mater. 15 (2016) 669–678.
[31] B. Zhang, B.F.L. Lai, R. Xie, L. Davenport Huyer, M. Montgomery, M. Radisic, Microfabrication of AngioChip, a biodegradable polymer scaffold with microfluidic vasculature, Nat. Protoc. 13 (2018) 1793–1813.
[32] M. Montgomery, L. Davenport Huyer, D. Bannerman, M.H. Mohammadi, G. Conant, M. Radisic, Method for the fabrication of elastomeric polyester scaffolds for tissue engineering and minimally invasive delivery, ACS Biomater. Sci. Eng. 4 (2018) 3691–3703.
[33] R.T. Tran, P. Thevenot, D. Gyawali, J.-C. Chiao, L. Tang, J. Yang, Synthesis and characterization of a biodegradable elastomer featuring a dual crosslinking mechanism, Soft Matter 6 (2010) 2449–2461.
[34] C.D. Morley, S.T. Ellison, T. Bhattacharjee, C.S. O'Bryan, Y. Zhang, K.F. Smith, C. P. Kabb, M. Sebastian, G.L. Moore, K.D. Schulze, Quantitative characterization of 3D bioprinted structural elements under cell generated forces, Nat. Commun. 10 (2019) 3029.
[35] S.V. Murphy, P. De Coppi, A. Atala, Opportunities and challenges of translational 3D bioprinting, Nat. Biomed. Eng. 4 (2020) 370–380.
[36] U. Blache, M.M. Stevens, E. Gentleman, Harnessing the secreted extracellular matrix to engineer tissues, Nat. Biomed. Eng. 4 (2020) 357–363.
[37] M. Machour, N. Hen, I. Goldfracht, D. Safina, M. Davidovich-Pinhas, H. Bianco-Peled, S. Levenberg, Print-and-Grow within a novel support material for 3D bioprinting and post-printing tissue growth, Adv. Sci. 9 (2022) 2200882.
[38] J. Zhang, B.J. Allardyce, R. Rajkhowa, Y. Zhao, R.J. Dilley, S.L. Redmond, X. Wang, X. Liu, 3D printing of silk particle-reinforced chitosan hydrogel structures and their properties, ACS Biomater. Sci. Eng. 4 (2018) 3036–3046.
[39] B. Majhy, P. Priyadarshini, A. Sen, Effect of surface energy and roughness on cell adhesion and growth–facile surface modification for enhanced cell culture, RSC Adv. 11 (2021) 15467–15476.
[40] S.Y. Boateng, T.J. Hartman, N. Ahluwalia, H. Vidula, T.A. Desai, B. Russell, Inhibition of fibroblast proliferation in cardiac myocyte cultures by surface microtopography, Am. J. Physiol. Cell Physiol. 285 (2003) C171–C182.

[41] D. Bannerman, S. Pascual-Gil, S. Campbell, R. Jiang, Q. Wu, S. Okhovatian, K. T. Wagner, M. Montgomery, M.A. Laflamme, L.D. Huyer, Itaconate and citrate releasing polymer attenuates foreign body response in biofabricated cardiac patches, Mater. Today Biol. 24 (2024) 100917.

[42] L. Davenport Huyer, B. Zhang, A. Korolj, M. Montgomery, S. Drecun, G. Conant, Y. Zhao, L. Reis, M. Radisic, Highly elastic and moldable polyester biomaterial for cardiac tissue engineering applications, ACS Biomater. Sci. Eng. 2 (2016) 780–788.

[43] M. Jeyhani, R. Thevakumaran, N. Abbasi, D.K. Hwang, S.S. Tsai, Microfluidic generation of all-aqueous double and triple emulsions, Small 16 (2020) 1906565.

[44] J.H. Lee, S.I. Protze, Z. Laksman, P.H. Backx, G.M. Keller, Human pluripotent stem cell-derived atrial and ventricular cardiomyocytes develop from distinct mesoderm populations, Cell Stem Cell 21 (2017) 179–194. e174.

[45] Y. Zhao, N. Rafatian, N.T. Feric, B.J. Cox, R. Aschar-Sobbi, E.Y. Wang, P. Aggarwal, B. Zhang, G. Conant, K. Ronaldson-Bouchard, A platform for generation of chamber-specific cardiac tissues and disease modeling, Cell 176 (2019) 913–927. e918.